2022

The Effects of an Ultrafast Pulsed Laser on YBCO Thin Film Circuit Transients

Matthew L. Rustad
Wright State University

Follow this and additional works at: https://corescholar.libraries.wright.edu/etd_all

Part of the Physics Commons

THE EFFECTS OF AN ULTRAFAST PULSED LASER ON YBCO THIN FILM CIRCUIT TRANSIENTS

A thesis submitted in partial fulfilment of the
Requirements for the degree of
Master of Science

By

MATTHEW L. RUSTAD
B.S., Wright State University, 2015

2022
Wright State University

WRIGHT STATE UNIVERSITY

GRADUATE SCHOOL

<u>April 6, 2022</u>

I HEREBY RECOMMEND THAT THE THESIS PREPARED UNDER MY SUPERVISION BY Matthew L. Rustad ENTITLED The Effects of an Ultrafast Pulsed Laser on YBCO Thin Film Circuit Transients BE ACCEPTED IN PARTIAL FULFILLMENT OF THE REQUIREMENTS FOR THE DEGREE OF Master of Science.

_____

Jason A. Deibel, Ph.D.
Thesis Director

_____

Jason A. Deibel
Chair, Department of Physics

Committee on
Final Examination

_____

Jason Deibel, Ph.D.

_____

Brent Foy, Ph.D.

_____

Ivan Medvedev, Ph.D.

_____

Barry Milligan, Ph.D.
Vice Provost, Academic Affairs; and Dean of
the Graduate School

Abstract

Rustad, Matthew L. M. S. Department of Physics, Wright State University, 2022. The Effects of an Ultrafast Pulsed Laser on YBCO Thin Film Circuit Transients.

Terahertz (THz) frequency light has shown promise for a wide variety of applications due to its material characterization and imaging capabilities. Its nondestructive nature coupled with its submillimeter spatial resolution provides the most value for terahertz light as an imaging tool. The application of terahertz technology has been limited by a lack of novel and powerful sources. It has been shown that that Yttrium Barium Copper Oxide (YBCO), a type II superconductor, has certain properties that would allow YBCO to be an effective source for THz light. Recent microwave work has shown that when a persistent supercurrent is placed on a thin film YBCO ring and is discharged, the decelerating electrons could produce THZ electromagnetic radiation. An ultrafast femtosecond laser incident on such a YBCO ring would disrupt the superconducting mechanism of the material. A series of tests examining YBCO and its optoelectronic properties were conducted. These included ultrafast pump-probe measurements, inspection of the discharging and charging rates, and finally time-domain terahertz emission experiments. The pump-probe measurements revealed electron relaxation times in the picosecond range. While it was shown that the ultrafast laser was able to induce and discharge a super current in the thin film superconductor, it was dependent on laser fluence and had no detectable wavelength dependence. However, no THz radiation was detected with the time-domain measurement system.

Table of Contents

List of Figures

1. Introduction

Terahertz (THz) spectroscopy is steadily becoming an important tool across many different scientific disciplines. The location of THz light on the electromagnetic spectrum, 30 μm to 3 mm or 100 GHz to 10 THz, provides several more useful properties of THz light. THz photons are low energy enough to be non-ionizing, are beneath the plasma frequency of metals, and are relatively loss-less in insulating plastics, all while being high enough in frequency to exhibit sub-millimeter spatial resolution for imaging.

The non-ionization property coupled with the submillimeter resolution of THz frequencies makes it a perfect tool for nondestructive evaluation (NDE). As the push for lightweight materials grows, such as foams, ceramics, and plastics (Reports and Data, 2020), the need for nondestructive evaluation also grows. A few examples that demonstrate the importance of nondestructive evaluation involves the use of THz radiation for inspection of the space shuttle external tank and orbiter following the Columbia (Karpowicz, 2005) tragedy and for determining the authenticity of paintings and other artwork (Goya, 2013).

THz radiation is generated either in a continuous wave (CW) or pulsed modality. CW THz is monochromatic and pulsed THz is broadband, with some sources capable of producing under 1 THz to nearly 7 THz (Paradis, 2018). Broadband radiation is the type of THz generation that is at the focus of the work described herein. A broadband terahertz source can be described as a single cycle transient generated over a picosecond time. The broadband THz pulse can be sampled in the time-domain while the frequency-dependent magnitude and phase information of the electric field THz signal are preserved and accessible via Fourier transform.

While THz time domain spectroscopy (TDS) is a powerful tool for imaging and spectroscopy, it has its drawbacks. The major hindrance, which limits THz technologies from

reaching their full potential, is the limited power of each pulse. The lack of photons in each pulse increases the exposure/detection time necessary to yield an image and/or spectroscopic data, the accumulation time of which can take from minutes to hours. For a stationary sample, the length of the measurement time is not much of an issue, but for the case of real time data needed for commercial or everyday use, it is a major hurdle for THz TDS. In order to combat this weakness, novel and more efficient and powerful sources for THz generation must be sought after.

A possible promising THz source is the Type II super conductor Yttrium Barium Copper Oxide (YBCO) (Bulmer et al, 2015). It is a well-known high temperature superconductor with a critical temperature of 93 K. YBCO has been well characterized, known London penetration depth for all axes of crystal orientation as well as coherence length of cooper pairs for axes, which will be discussed in the section on supercondivity. Manufacturing of YBCO is also very well understood and can be stoichiometrically optimized to have the highest possible critical temperature allowable by the material. (Benzi, P., 2004)

This thesis focuses on determining how a current is induced and discharged on a superconducting YBCO thin film using an incident femtosecond pulse from an ultrafast laser. The discharge of a current on a YBCO thin film has been hypothesized to produce broadband THz radiation with a bandwidth that will stretch from the radio frequency (RF) to the far-infrared, including terahertz frequencies. An antenna such as this has been estimated to yield upwards of six orders of magnitude of power beyond current conventional methods. Preliminary experimental evidence is promising (Bulmer et al, 2015).

Inspired by these ideas, a time domain experiment was designed to determine if pulsed THz radiation could be generated from a potential YBCO antenna. THz generation is proportional to the change in current density as a function of time, $E_{THz} \propto \frac{d\vec{J}}{dt}$. The pulsed laser would disrupt the

super current by breaking cooper pairs, superconducting electrons, and excite those electrons into the conduction band. Tonouchi et al. demonstrated that a bowtie antenna configuration on a YBCO thin film produced terahertz radiation using a pulsed Ti:Sapphire laser. They were only able to generate THz when the antenna was placed within a magnetic field, utilizing the trapped magnetic flux within the superconductor. It was believed that a YBCO ring could also generate THz radiation utilizing a pulsed laser without using a biased current as the induced current from the trapped flux is already contained within the superconducting ring.The superconducting thin film will first be characterized using ultrafast pump-probe spectroscopy in order to determine the YBCO's electronic relaxation times. The YBCO will then be charged using two methods; the first method consists of using a Ti:Sapphire laser incident on the thin film in the presence of a magnetic field, and the second method used will be using a magnetic field strong enough to penetrate through the material to induce a current. The YBCO thin film will then be discharged with the use of a Ti:sapphire laser without a magnetic field present.

2. Terahertz Radiation Generation

Broadband THz radiation can be generated through a variety of techniques. The method used in these experiments incorporated the use of an ultrafast Ti:Sapphire laser and a photoconductive antenna or PCA. The role of an ultrafast laser in the generation of THz from a PCA is to provide the photon energy required for the electrons in the antenna substrate of gallium arsenide (GaAs) to be excited from the valence band to the conduction band. The ultrafast pulse creates pulsed THz which provides a broadband time domain signal. Concordantly, using a slight variation of the same principle a PCA can also be used as a THz detector. Before THz generation is discussed any further, it is important to take a closer look at the ultrafast laser we used and its role in generating broadband single pulsed THz radiation.

The Ultrafast laser used in these experiments is a Coherent Chameleon Ultra II Ti:Sapphire pulsed laser. It has a repetition rate of 80 MHz, a pulse width of approximately140 fs, and a tunable center wavelength (from 680 nm to 1080 nm) with 10 nm of bandwidth at full width half maximum (FWHM). A repetition rate of 80 MHz corresponds to 80 million pulses per second or one pulse every 12.5 ns, with each pulse in the pulse train being identical. While at 800 nm the Chameleon Ultra II can produce greater than 3.5 W of power with roughly 44 nW per pulse. The time between pulses is far greater in duration than the length of the pulse, by roughly five orders of magnitude.

The two most commonly used emitters and detectors of THz radiation used in conjunction with a Ti:Sapphire laser are PCA's and Electro-optic (EO) crystals (Tani, M., 2002). The known THz emitters used in these experiments were both PCA's. The commercial THz TDS system utilizes a dipole antenna consisting of Ti/Au alloy lithographically fabricated transmission lines deposited on a semi-insulated GaAs substrate of GaAs as an emitter and a low temperature

grown gallium arsenide (LT-GaAs) PCA as a detector and the lab built THz TDS system uses a

p-doped indium arsenide (InAs) PCA and a zinc telluride (ZnTe) EO detector. LT-GaAs has a

drastically reduced carrier lifetime. In both of these experiments, the ultrafast laser was used by

the PCA's to emit THz radiation. The LT-GaAs and ZnTe detectors also used the ultrafast laser

to detect the incoming THz radiation.

Using optically pumped PCAs to generate broadband THz radiation was first accomplished

in the late 1980s by THz pioneers David Auston (Auston, D., 1983) and Daniel Grischkowsky

(Fattinger, C., 1988). A PCA consists of a photoconductive substrate with a DC biased dipole

antenna on its surface, Figure 2-1. When the ultrafast laser is incident on the photoconductive

substrate, as the name suggests, electrons are excited from the valence band to the conduction

band. GaAs has a band gap of 1.42 eV and the 800 nm light from the Ti:Sapphire laser has a

photon energy of 1.55 eV. The conduction band electrons or photocarriers are now free to move

and are accelerated by the electrical potential from the dipole inducing a transient photocurrent.

THz radiation is generated proportionally to the changing current, $E_{THz} = \frac{\partial J}{\partial t}$. This time-varying

photocurrent in the dipole antenna results in the emission of pulsed THz frequency radiation

(Burford, N., 2017). In an alternative approach to THz generation, the p-InAs PCA takes

advantage of a phenomenon called the photo-Dember effect. The photo-Dember effect is a

surface emission mechanism based on carrier dynamics similar that with a GaAs PCA. Instead of

using an external electric potential, THz radiation is generated due to the intrinsic surface electric

field which naturally exists in InAs due to the PD effect. The surface field caused by the PD

effect has interesting consequences when an ultrafast laser is incident on its surface. The

electrons are excited out of the valence band and into the conduction band and the internal

electric field induces a photocurrent within the material. The photocurrent is due to the

difference between the electron and electron hole mobilities and the symmetry break at the surface gives rise to a dipole (Apostolopoulos, V. 2014).
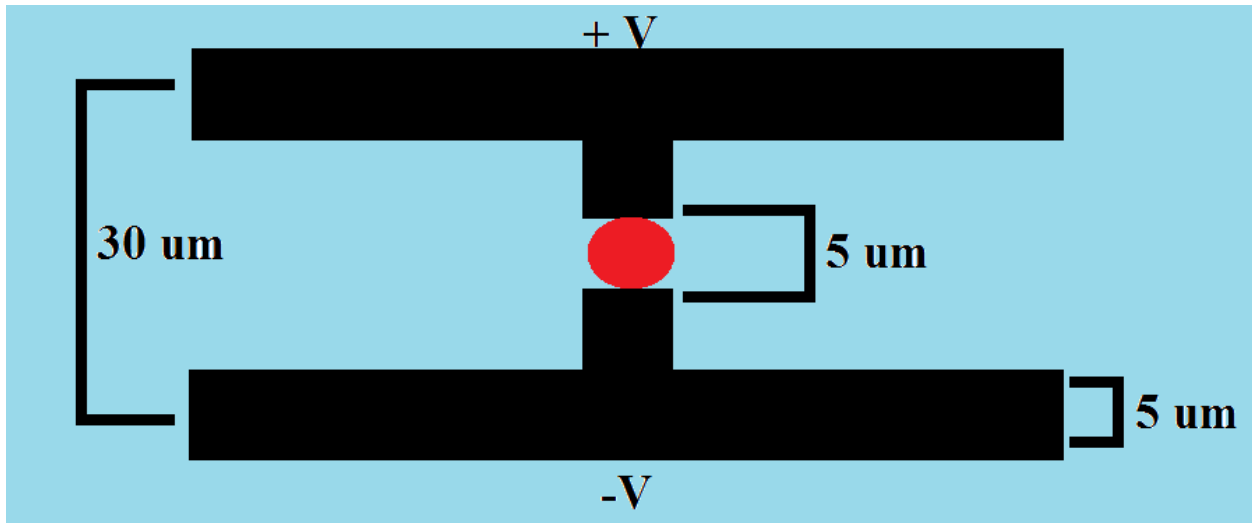
Figure 2-1. Ulatrashort laser pulse illuminates the gap between the transmission lines of the dipole antenna. The laser moves electrons from the valance band to the conduction band allowing the "freed" electrons to move in the direction of the electrical potential.

Broadband THz detectors can be broken down into two main groups; thermal detectors, mainly bolometers, and pulsed detectors, typically used for TDS. A bolometer measures the power of THz radiation via the change in temperature. Bolometers are often cooled to maximize their change in temperature, which increases the signal output. Since bolometers measure power, gathering phase information can be quite difficult. Whereas pulsed detectors measure the electric field in time keeping the phase information intact. Detection of the THz radiation generated by a commercial unit (Figure 2-2 and Figure 2-3, which utilizes a smaller time window) is accomplished with a similar method, a PCA built on LT-GaAs. LT-GaAs is better suited as a detector than GaAs due to its higher resistivity, higher carrier mobility, and lower carrier lifetime (Harmon, E.S.). A split-off pulse from the same ultrafast laser is also utilized in the detection scheme as well as the generation. Instead of using an external dipole to create the electrical the potential, the THz radiation is the source of the electric field. The incident laser generates

photocurrent by providing the energy required to "place" the electrons in the conduction band and the electric field from the THz provides the potential to move the electrons. The current is quite weak (sub-nanoamp) then measured and amplified.
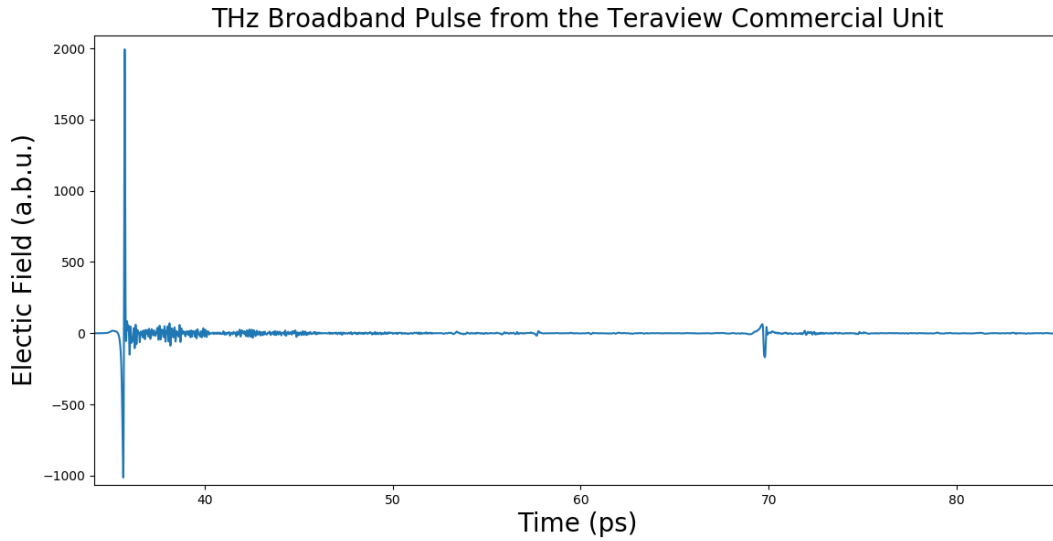
Figure 2-2. THz pulse generated by GaAs and detected by LT-GaAs in the Teraview commercial system.
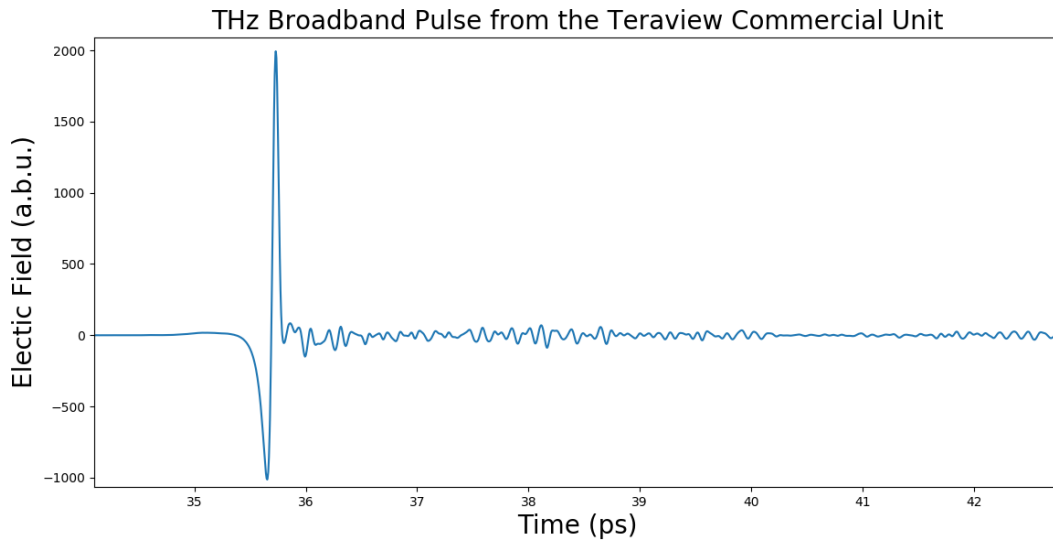
Figure 2-3. Close up of the THz pulse generated by the Teraview commercial system.

An alternative method uses Zinc Telluride (ZnTe), an electro-optic crystal, to detect THz radiation. In this scheme. A $< 1,1,0 >$ oriented ZnTe crystal experiences an electric-field

induced optical birefringence when THz radiation is incident on the crystal and polarized in the direction of the crystal lattice (Wu, Q., et al, 1996). This causes a change in polarization of light being transmitted through it, such as the ultrafast laser (we will call this the probe beam). The degree of change in the polarization of the ultrafast laser is linearly proportional to the strength of the electric field of the THz radiation. In order to achieve high sensitivity detection of THz light, a differential detection scheme is utilized. After passing through the crystal, the linearly polarized probe beam passes through a $\frac{\lambda}{4}$ wave plate, which circularly polarizes the probe beam. The vertical and horizontal components of the circularly polarized beam are separated by a Wollaston prism and then measured by a pair of identical photodiodes, one for the vertical and one for horizontal polarization. If the beam perfectly is circularly polarized, both photodiodes generate the same voltage signal. The THz pulse is focused onto the ZnTe crystral using a series of gold-coated parabolic mirrors. The THz electric-field induces a change in the polarization in the probe beam corresponding to a change in vertical and horizontal components of the polarization, which creates more voltage in one photodiode than the other. The photodiode voltage is then sent to a lock-in amplifier and subtracted. The result being the electric field of the THz radiation at a given time.
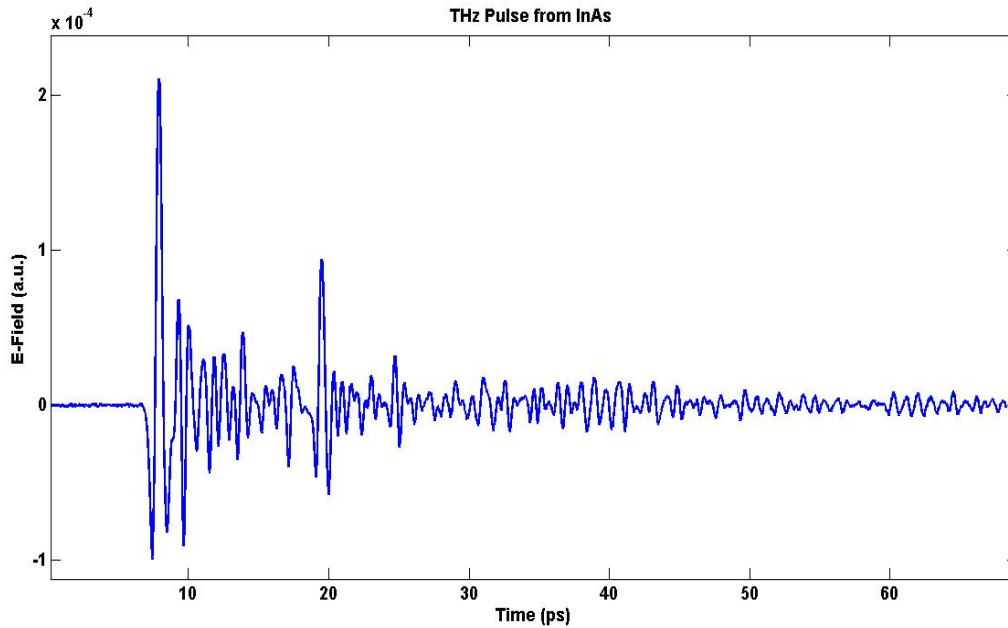
Figure 2-4. Measured THz electric field from p-doped InAs measured using a ZnTe crystal.

As previously discussed, the ultrafast pulsed laser is used to create and detect THz radiation. The laser is split using a polarized beam splitter into a pump beam (for the THz source) and a probe beam which samples the THz pulse. A $\frac{\lambda}{2}$ wave plate is placed before the beam splitting cube to control the amount of laser power in each beam. The pump beam and probe beam must travel the same distance to measure the THz pulse. Keep in mind the pulse lasts roughly 50 ps (corresponding to 15 mm in travel) and the time between pulses is 12.5 ns, meaning the pulse spends more time off than on. After the path lengths are within 1.5 cm of each other, a delay rail is used by the pump path to increase or decrease the length of travel by the probe beam to match the length of the probe path. The purpose of the delay rail is to sample the entirety of the pulse by changing the path length of the pump beam.

The cutting edge of THz detection is kinetic induction detection which utilizes thin film superconductors. THz photons contain enough energy to break cooper pairs which changes the surface inductance of the superconductor. Superconductors maintain their current indefinitely

9

unless acted upon or their temperature is raised above their critical temperature. This results in a proportional relationship between the change in surface inductance and change in the number of quasiparticles. Kinetic induction detection is currently being used for astronomical measurements in the sub-millimeter range. (R A Lewis, 2019)

3. Superconductors

A superconductor is any material that can achieve perfect conductivity when cooled below a certain temperature, which is referred to as its critical temperature, T_c. A material is considered a perfect conductor when it has absolutely zero electrical resistance. Even commonly used conductors such as copper or silver have some resistance roughly in milliohms, which is dependent on temperature and cross-sectional area, a value low enough to be considered zero when a voltage source is applied. Once the source is removed, any residual electric current in the material quickly dissipates. For a superconductor, this current can flow indefinitely, commonly referred to as a persistent current, as long as the material remains in its superconductive state. A persistent current has been observed to exist in a superconducting loop without any measurable loss for years. It is anticipated that there will be no measureable change in the magnetic field from a supercurrent for over 10^5 years. (Tinkerham, M, 2015).

The first documented observation of perfect electrical conductivity was observed by Kamerlingh Onnes in 1911. Onnes was attempting to measure the resistance of various materials at temperatures as close to absolute zero as he could obtain. It was thought that resistivity in a material would approach zero as the temperature decreased and would jump to infinity at absolute zero. When Onnes cooled mercury using liquid helium, which has a boiling point of 4 Kelvin, a slight drop in resistance was expected, but the resistance instead immediately dropped to zero. (Delft, D and Kes, P, 2010) The sudden drop in the resistivity of mercury perplexed Onnes and ushered in a new field in physics.

The idea of a persistent current inspired studies involving the magnetic properties of superconductors. In 1933, Meissner and Ochsenfeld observed the existence of perfect diamagnetism in superconductors. (Delft, D and Kes, P, 2010) A diamagnet is any material

which repels a magnetic field, which is numerically defined as having a magnetic permeability less than μ_0, the permeability of free space. When superconductors are below their critical temperature, they produce a screening current in response to a magnetic field. This screening current produces a magnetic field in the opposite direction to cancel out any magnetic field which exists within the superconductor. This screening effect was thought to be explained by the perfect conductivity aspect of a superconductor. Materials do not like to experience a change in magnetic flux. Magnetic flux is the amount of magnetic field lines which exist in an enclosed area. In response to a changing magnetic flux, a conductor will generate a current to oppose such a change. Due to its perfect conductivity, a superconductor can screen out currents very well. However, this is not the entirety of the story.

If a magnetic field is present inside a superconductor when it is cooled below its critical temperature the magnetic field will be completely dispelled from the material. (Meissner, W., and Ochsenfeld, R, 1933) This property is known as the Meissner effect and cannot be explained by the perfect conductor aspect of superconductivity. It is energetically favorable for a superconductor to find an equilibrium state where the sum of the kinetic, magnetic, and condensation energies are at a minimum. For the superconductor, this corresponds to the expulsion of magnetic flux. (De Gennes, P, 1999)

When a superconducting ring expels magnetic flux, a current is induced. Due to the zero resistance nature of a cooled superconductor, the induced current is the previously mentioned persistent current or supercurrent. This supercurrent produces the amount of flux the material expelled in its transition to its superconductive state, up to the number of superconductive electrons at its disposal. The persistent current is the result of the superconductive electrons forming into pairs consisting of opposite spins and momentum, referred to as Cooper pairs.

Although cooper pairs consist of two electrons (fermions), they obey Bose—Einstein statistics, meaning they act as bosons when the electrons are paired up in this manner. Since the cooper pairs are bosons, they condense into a ground state in which the phase and wave vector form a coherent macroscopic wave function. (White, G., and P. J. Meeson, 2006)

These electron pairs work together to maintain an equilibrium between repulsion and attraction. The first electron alters the location of the positive nuclei, or lattice points in the crystal. This interaction pulls the positive nuclei towards the electron via coulombic forces and creates a positive potential well in its wake. The potential well "tugs" the subsequent electron, which in turn is repelling the preceding electron. (Bardeen, J., et al, 1957)
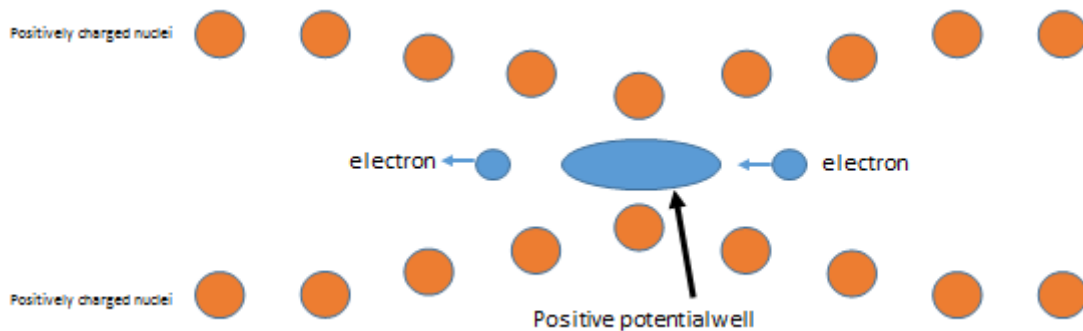
Figure 3-1. A superconductive electron deforms the crystal lattice and creates a positive electrical potential well in its wake. A second electron is attracted to the well and follows behind the first electron while also being repelled by it. When the two forces are in equilibrium a Cooper pair is formed.

Cooper pairs have a characteristic length referred to as the superconducting coherence length. The superconducting coherence length, ξ, is commonly referred to as the size of the cooper pair and is described by Equation (3.1), where v_F is the fermi velocity and E_g is the energy band gap of the superconductor. (Bardeen, J., et al, 1957) The description of the band gap in a superconductor is quite different than for semiconductors. Unlike a semiconductor, the band gaps do not occur at the Brillouin zone boundary, as they are not permanently fixed in place within the

crystal lattice. The band gap of a superconductor is in relation to the fermi energy and the cooper pairs and not the nuclei of the lattice.

$$\xi_0 = \frac{-2\hbar v_F}{\pi E_g} \tag{3.1}$$

There is a second characteristic length used in describing superconductors known as the London penetration depth. The "perfect" diamagnetism of superconductors, discussed earlier, is not entirely accurate. In fact, a magnetic field does penetrate into a superconductor. However, its strength exponentially decays rapidly as a function of depth, and the penetration depth of the magnetic field is typically on the order of a 100 nm, described by equation (3.2). (Bardeen, J., et al, 1957) where m is the mass of the electron, c is the speed of light, n is the number density of

$$\lambda_L(0) = \left(\frac{mc^2}{4\pi ne^2}\right)^{1/2} \tag{3.2}$$

free superconducting electrons, e is the charge, and $\lambda_L(0)$ is the penetration depth at absolute zero. The temperature dependent penetration depth is then described by equation (3.3). The

$$\lambda_L(T) = \frac{\lambda_L(0)}{\left(1-\left(\frac{T}{T_c}\right)^4\right)^2} \tag{3.3}$$

magnetic field exponentially drops off as a function of the distance into the superconductor and the temperature dependent penetration depth acts as a constant which describes the decay rate. When discussing bulk superconductors, it is safe to describe them as perfect diamagnets,

$$B = B_0 exp\left(\frac{-x}{\lambda_L(T)}\right) \tag{3.4}$$

however, the situation becomes more complicated when using a thin film superconductor that has a thickness approximately equal to or less than the London penetration depth.

3.1 Type I Superconductors

There are two types of superconductors, commonly referred to as Type I or Type II. Type I superconductors are typically pure elements and have very low critical temperatures. However,

Element	Critical Temp. (K)	Element	Critical Temp. (K)
Zinc	0.855	Tin	3.72
Aluminum	1.2	Mercury	4.15
Uranium	1.8	Vanadium	5.03
Indium	3.4	Lead	7.19

Table 3-1. List of elemental Type I superconductors and their critical temperatures.

these are not the qualities that define a Type I superconductor. A material is defined as a Type I or Type II superconductor based on the relationship of the ratio of their characteristic lengths; magnetic field penetration depth and coherence length. If $\kappa = \lambda/\xi$, a Type I superconductor is then defined by the inequality, $0 < \kappa < 1/\sqrt{2}$ and as a type II by $\kappa > 1/\sqrt{2}$. (Tinkham, M, 2015) This relationship is the result of some defining material properties between the two types of superconductors, most notably how they interact with magnetic fields, London penetration depth, λ, and the stability of their cooper pairs, coherence length, ξ.

All superconductors have an upper critical magnetic field, H_{c1}. It is where a magnetic field is so strong it destroys the superconductive state and the material returns to its normal state regardless of the material's temperature. As previously discussed, if a material can attain a superconductive state, it will do so because it is more energy efficient to expel the internal magnetic fields. The screening current forms in the presence of a magnetic field has a kinetic energy associated with it. When the kinetic energy of the superconducting electrons which make up the screening current, is greater than the energy "saved" by the material transitioning into a superconductive state it is no longer energy efficient to be in said superconducting state and the

material loses its superconductivity. (Landau Lev Davydovič, and Pitaevskij Lev Petrovič, 1981)

The total energy saved by transitioning to a superconductive state is described by Equation 3.5, where f_{London} is the London free energy, m is electron mass, n_c is electron number density, v_s is the velocity of the superconducting electrons, and $\frac{B^2}{2\mu_0}$ is the magnetic energy.

$$f_{London} = \int \left(\frac{1}{2}mn_cv_s^2 + \frac{B^2}{2\mu_0}\right)dV \qquad (3.5)$$
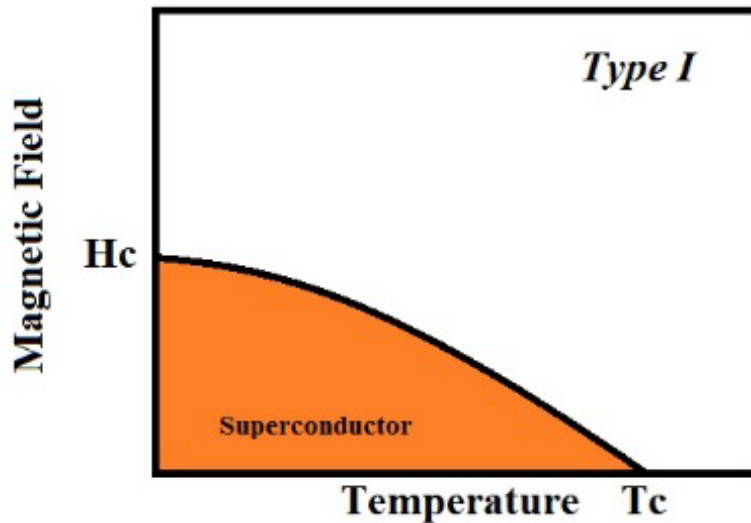
Figure 3-2. A Type I superconductor has temperature dependent critical magnetic field. When a superconductor is exposed to magnetic field above this value the material will transition out of its superconductive state.

Type I superconductivity has been characterized and modeled by Bardeen, Cooper, and Schrieffer; this model is known as BCS theory. In order to correctly address the superconductivity phenomena, BCS theory must explain the following: the phase transition to superconductivity at a critical temperature, how electronic specific heat varies with temperature, the Meissner effect, infinite conductivity, and the dependence of T_c on atomic mass. Their theory of superconductivity, and now the generally accepted theory, describes the previously stated electron-phonon interaction. When the attractive force from the potential well, caused by the lattice deformations, overcomes the repulsive force between the two electrons making up the

cooper pair, a material is said to be in a superconductive state. (Bardeen, J., et al, 1957) It is this phonon interaction which is responsible for the five listed type I superconductive phenomena.

BCS theory does not properly address the functionality of type II superconductors. There are significant differences between Type I and Type II superconductors which result from the increased ratio of a Type II's penetration depth to its coherence length. Type II superconductors make up all of the high temperature superconductors, but not all Type II's are high temperature. A high temperature superconductor commonly has a T_c greater than 30 K. This is primarily due the discovery of Lanthanum Barium Copper Oxide, $La_{2-x}Ba_xCuO_4$, in 1986 which has a T_c of 30 K, which had the highest discovered critical temperature at the time. (Kadin, A 1999,) The current record for highest critical temperature at atmospheric pressure is held by a cuprate, Mercury Barium Calcium Copper Oxide, $HgBaCaCuO$ at 138 K.

3.2 Ginzburg-Landau Equations

Ginzburg-Landau (GL) theory (1950) was originally used to describe the second order phase change (superconductivity) for Type I superconductors macroscopically. It was not until 1957, with the formulation of BCS theory, was there a microscopic explanation for the superconducting phenomena. GL theory begins with the previously mentioned free energy of the superconductor at the transition (or condensation) point. F_n is the free energy of the normal state

$$F = F_n + \int \left\{ \frac{\hbar^2}{4m} |\nabla\psi|^2 + a|\psi^2| + \frac{1}{2}b|\psi|^4 \right\} dV \tag{3.6}$$

where $\psi = 0$, b is dependent on the density of the material, and a represents the temperature of the material in relation to the critical temperature where $a = \alpha(T - T_c)$. In the absence of a magnetic field the free energy equation reduces to Equation 3.7:

$$F = F_n + \left\{ aV + \frac{1}{2}b|\psi|^4 \right\} \tag{3.7}$$

When an external magnetic field is considered for the free energy equation for a superconductor we arrive at Equation 3.8, where F_{n_0} is the free energy of a material in the

$$F = F_{n_0} + \int \left\{ \frac{B^2}{8\pi} + \frac{\hbar^2}{4m} \left| \left(\nabla - \frac{2ie}{\hbar c} A \right) \psi \right|^2 + a|\psi|^2 + \frac{1}{2} b|\psi|^4 \right\} dV \qquad (3.8)$$

normal in the absence of a magnetic field. After minimizing the free energy and executing the volume integral, we arrive at Equation 3.9. When this equation is varied with respect to the

$$\frac{1}{4m} \left(-i\hbar\nabla - \frac{2e}{c} A \right)^2 \psi + \alpha\psi + b|\psi|^2\psi = 0 \qquad (3.9)$$

external fields vector potential, A, it gives rise to Maxwell's equation. Where the current density

$$\nabla \times B = \left(\frac{4\pi}{c} \right) j \qquad (3.10)$$

j is represented by Equation 3.11. Equations 3.9-3.11 represent the complete set of GL equations.

$$j = -\frac{ie\hbar}{2m} (\psi^*\nabla\psi - \psi\nabla\psi^*) - \frac{2e^2}{mc}|\psi|^2 A \qquad (3.11)$$

The set of GL equations provide the functions which describe of characteristic lengths previously discussed, penetrations depth and coherence length. When Equation 3.11 is substituted into Equation 3.10 and the curl of both sides are taken and $|\psi|^2 = \alpha(T - T_c)b$, for small magnetic fields

$$\nabla \times \nabla \times B = -\Delta B = \nabla \times \left(\frac{4\pi}{c} \right) \left(-\frac{ie\hbar}{2m} (\psi^*\nabla\psi - \psi\nabla\psi^*) - \frac{2e^2}{mc}|\psi|^2 A \right) \qquad (3.12)$$

we arrive at Equation 3.12. When line integrated through the superconductor we arrive back at

$$\Delta B = B \left(\frac{4\pi e^2 n_s}{mc^2} \right) \qquad (3.13)$$

Equations 3.1-3.3. The second characteristic length is the coherence length of the superconductor and it essentially describes the "size" of the Cooper pair. The Cooper pair correlation length is not effected by an external magnetic field, meaning we can start with the free energy equation in the absence of a magnetic field, Equation 3.8. Using the formulations from Landau on the

Fluctuations of the Second Order Parameter, we come to Equation 3.14, $\alpha = a(T_c - T)\psi^2$,

meaning coherence length, like penetration depth, is temperature dependent.

$$\xi = \sqrt{\frac{\hbar^2}{4m|\alpha|}} \tag{3.14}$$

GL offered an in depth macroscopic view of the second order phase change that is

superconductivity, but it also provided clues to a second type of superconductor. By analyzing

the surface tension at the phase transition from normal to superconducting we can see a defined

boundary where the surface tension changes from positive to negative. This boundary occurs

at $\lambda\sqrt{2} = \xi$. If the left hand side of this equation is greater, then the surface tension is negative

and the material is a Type II superconductor and if the right side is greater the material is a Type

I.

3.3 Type II Superconductors

Type I and Type II superconductors behave in the same fashion when in the absence of a

magnetic field. They both behave as perfect conductors and exhibit perfect diamagnetism.

However, the differences in their characteristic lengths are clearly observable when placed in a

strong enough magnetic field. Type II superconductors have a temperature dependent upper and

lower critical magnetic field. The upper critical magnetic field being synonymous to the critical

magnetic field of the Type I superconductor where the super conductive state is destroyed.

Below the lower critical magnetic field, Type I and Type II superconductors also behave
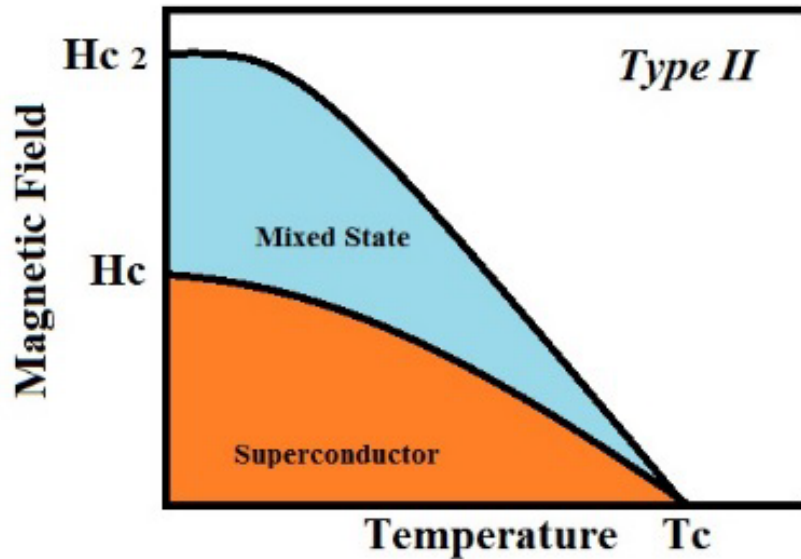
Figure 3-3. A type II superconductor has two critical magnetic fields boundaries. If a Type II superconductor is exposed to a magnetic field greater than H_{c_1}, it transitions into a mixed state where quantized magnetic flux is allowed to pass through the material. If the B-field is greater than H_{c_2} the material is no lonbger in a superconductive state, just like a Type I.

similarly. It is between the critical magnetic fields in which the Type II superconductors become distinctly different from their Type I counterparts.

Due to the difference in the ratio of the characteristic lengths, in which $\kappa > 1/\sqrt{2}$, when a Type II superconductor is placed in a magnetic field between H_{c1} and H_{c2}, the lower and upper critical fields respectively, the superconductor exists in a mixed state. (Kadin, A, 1999) While in a mixed state it is energetically favorable for the superconductor to allow magnetic flux to pass through it. The flux passing through the superconductor is quantized and begins when the external magnetic field is at H_{c1}. At the location where magnetic field lines pass through the superconductor a current forms around it creating a current vortex. As the applied magnetic field grows in strength, more vortices form until the electrons which make up the screening currents are now used by the vortices, and the material is no longer in its superconductive state.

The flux vortices can occur at any location on the superconductor and in a pure material can move to any location in an effort to stay evenly spaced due to coulombic forces. (J. Bardeen, M. J. Stephan, 1965) In an imperfect superconductor, the vortices form at locations where the superconductivity is at its weakest, where the impurities are located. The flux is considered to be pinned and cannot move to another location, and this phenomenon is known as flux pinning. (Matsushita T., 2007) When flux pinning occurs, a superconductor can be reoriented within a magnetic field and will remain in that orientation until acted on again.

3.4 YBCO

Perhaps the most widely used and studied Type II superconductor is Yttrium Barium Copper Oxide or YBCO. YBCO has important place in the history of superconductivity. It was first created in 1983 and was the first known superconductor with a critical temperature above the boiling point of liquid nitrogen. (Wu M. K., 1987) Liquid nitrogen is far easier to work with and much cheaper than liquid helium, opening the door for more research into high temperature superconductors. The most common form of the YBCO crystal is $YBa_2Cu_3O_{7-\delta}$, the δ represents the varying oxygen content this form can have.

YBCO crystalizes into a form similar to a perovskite structure, with the oxygen at the edge centers of the unit cell. The unit cell sizes are $a = 3.8067$ Å, $b = 3.8821$ Å, $and\ c = 11.6789$ Å. (Varshney, D., 2011) The cell is not uniform which means the characteristic lengths vary depending on which plane of the unit cell that is being interacted with. The most superconductive plane, the plane with the longest coherence length and the shortest penetration depth, is the a-b plane. More specifically the copper oxide plane. Single crystal YBCO has shown different results for a-axis and b-axis penetration depths, 160 nm and 80 nm respectively at 0 K. (Prozorv, R, et al., 2000) The superconducting electrons travel in the a-b plane so an average of the two

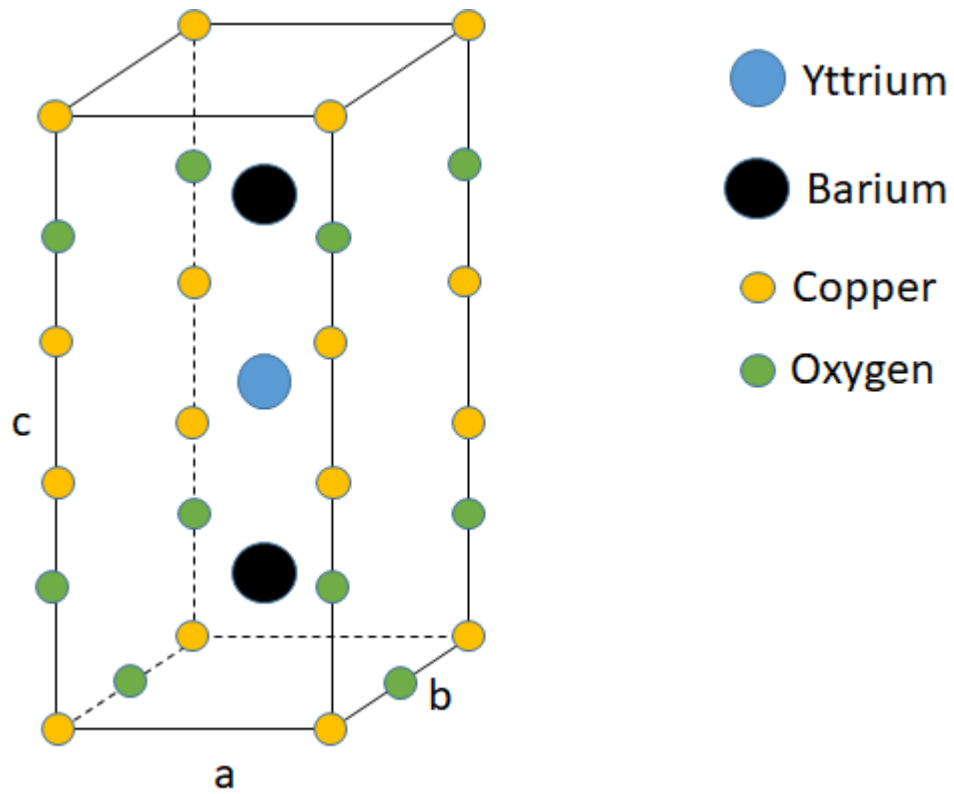values is expected. With the actual value from Prozorz et al being 145 nm at 0 K and 185 nm at

77 K.

Figure 3-4. YBCO unit cell dimensions. $a = 3.8067$ Å, $b = 3.8821$ Å, and $c = 11.6789$ Å.

4. Experiments

In this chapter the various experiments which were conducted will be described in detail. Which will include why the experiment was chosen, the experimental design, and how the experiment was conducted. There were six experiments in total. They are pump-probe spectroscopy, Time Domain THz emission, and the rest of the experiments inspected the rate at which the current was charged and discharged as a function of the laser's wavelength and power as well as the maximum current induced on the YBCO by increasing the magnetic field strength. Both the pump-probe spectroscopy and the TDS experiments required known materials to verify the experimental setup. In this case GaAs and p-doped InAs respectively.

4.1 Pump-Probe Spectroscopy

Pump probe measurements utilize an ultrafast pulsed laser to investigate the time-dependent electron dynamics of a material. The Ti:Sapphire laser used is a pulsed laser centered around 800 nm with a repetition rate of 80 MHz and pulse width of a 120 fs. The beam is split into vertical (pump beam) and horizontal (probe beam) polarization by a cube splitter. The pump beam illuminates and excites the electrons in the sample and the probe beam detects any changes in reflectivity in the sample. A change in reflectivity occurs when the energy of the photon is greater than the energy of the band gap. This causes the electron to jump to a higher energy level, which is referred to as the conduction band. When a material's electrons are excited into the conductive band the material's conductivity increases, thereby increasing its reflectivity and decreasing its transmissivity.
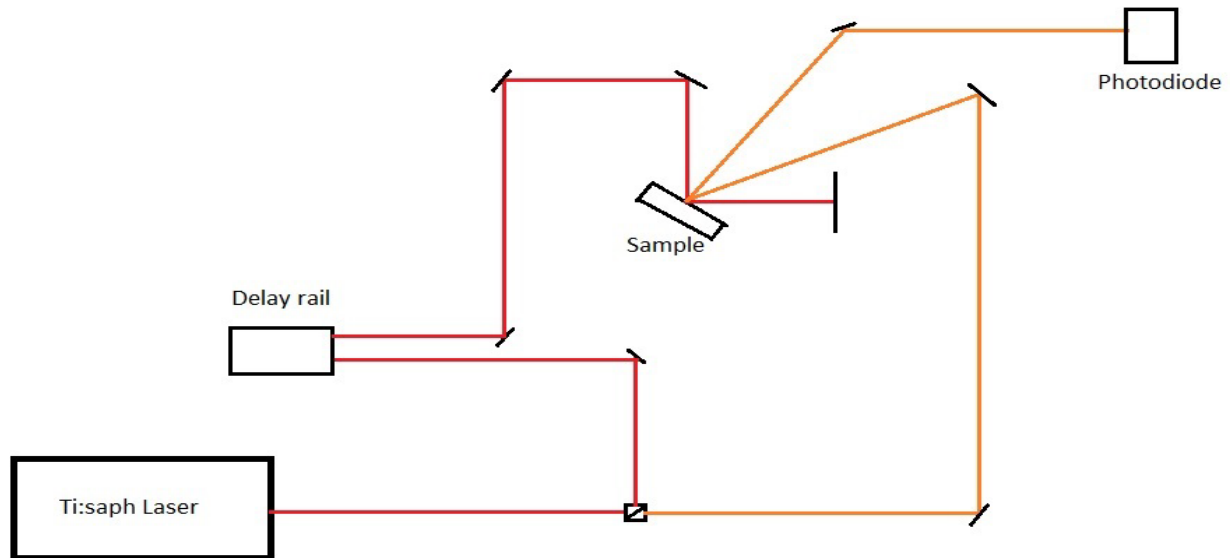
Figure 4-1. The Ti:sapphire laser is split into S and P polarizations. The pump beam (red) is then sent to a delay rail and then the sample. The probe beam (orange) travels down a path that is equal in length to the path the pump beam travels. They are both focused onto the sample and overlapped.

The true power of pump probe measurements comes from its ability to time resolve the electron excitation and relaxation times. Since the Ti:sapphire laser is pulsed at an 80 MHz repetition rate, one pulse every 12.5 ns, and has a pulse width of 120 fs, it is a great tool in the detection of electron excitation and relaxation. Electrons typically have a relaxation time in picoseconds (ps) and due to the relatively large gap between pulses and small time window of the pulse the laser is able to time resolve the electrons excitation and decay. When the pump pulses and probe pulses are lined up in time the pump beam path length is changed via the delay rail. Using the change in path length along with the speed of light the signal is converted to the time-domain.

The pump probe system was first evaluated by measuring semi-insulated Gallium Arsenide (GaAs). GaAs is a photoconductive direct bandgap semiconductor, it can be switched between conductor and insulator states depending on the conditions it is placed in. When the laser pulse is incident on the GaAs, electrons can excite across the energy gap from its insulator state to its

conductive state, if enough photon energy is present. The Ti:sapphire laser is centered around 800 nm, which correlates to 1.55 eV of photon energy. The band gap of GaAs is 1.424 eV, which is small enough to allow the laser to excite GaAs valence electrons to their conductive state.

A 500 μm thick GaAs wafer was placed in our cryostat, a cryostat is an apparatus which aides in experimentation at cryogenic temperatures by isolating the sample in a vacuum while allowing the cryogen, in this case liquid nitrogen (LN2), to cool the sample by convection. While it is not necessary for GaAs to be cooled to detect any changes in reflectivity, it is necessary to place it in the same conditions as the YBCO sample to prove that the quartz window of the cryostat will not hamper the detection scheme. The pump beam was set at an average power of 1.2 W and the probe beam at an average power of 20 mW, and was focused on the GaAs sample.

To increase the SNR the beams need to be focused as tight as possible (approximately 10's of microns) and precisely overlapped. The beam was focused using plano-convex lenses placed on micro-positioning stages as well as placing the cryostat on a 3-dimensional micro-positioning stage. Using an IR viewer and neutral density filters to reduce the intensity of the beam the laser spot on the sample was reduced by adjusting the focusing lenses. The same process was used to adjust the overlap of the pump beam and probe beam. By observing the spots through the IR viewer and periodically blocking one of the beams, a good approximation of the overlap was achieved. However, in order to improve the focus and the overlap of the beams the delay rail was placed at the peak signal displayed by the lock-in amplifier. Then slight adjustments to the 3-dimensional micro-positioning stage for the cryostat and focusing lenses were made until the signal was at its maximum value.

The reflected probe beam was directed to an amplified photodiode. The photodiode voltage was read by a Stanford Research Lock-in Amplifier which "locks in" to the frequency of the

optical chopper. An optical chopper is a rotating disk with notches large enough for a laser to pass through it. The control box for the optical chopper controls the frequency at which the beam is chopped and is connected to the lock-in amplifier. The lock-in amplifier is then "locked in" to that frequency, in this case 2000 Hz. A lock-in amplifier can extract data from extremely noisy environments by taking advantage of the fact that noise exists over a wide range of frequencies. If the signal has a definite frequency then the lock-in amplifier acts as a band pass filter and eliminates all signals outside of the frequency of the chopped light. To further reduce any noise present the delay rail was scanned seven consecutive times and averaged together. (screen pump light with different pol)
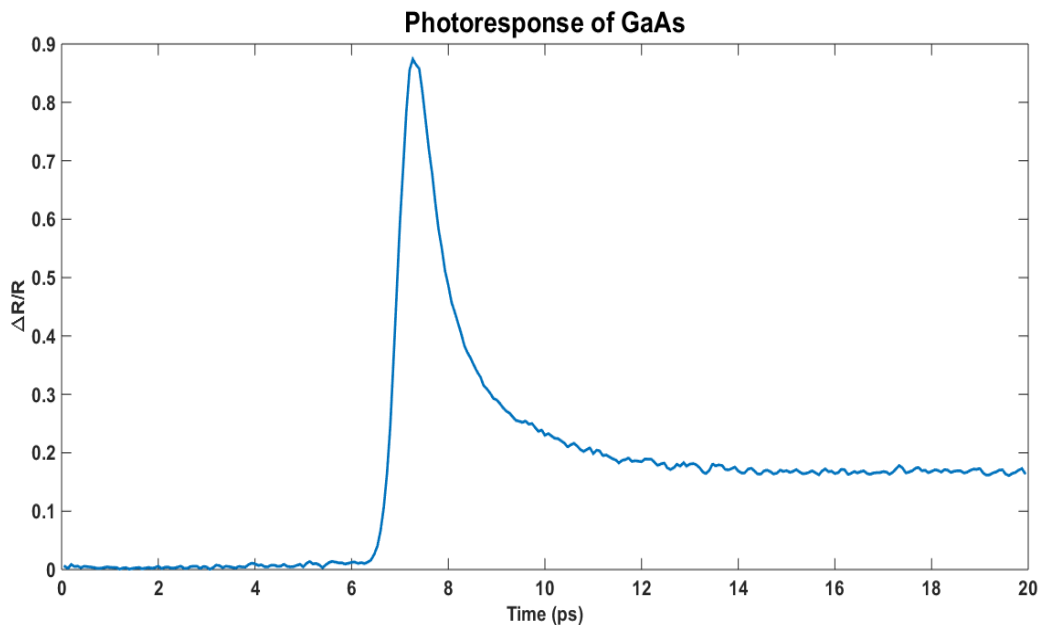

Figure 4-2. The change in reflection of GaAs due to excited electrons from an 800 nm laser pulse.

The graph shown in Fig 4-2 is the result of the pump-probe spectroscopy on GaAs. It shows the change in the reflection coefficient for GaAs vs time. The quick rise in the signal is the result of the excitation pulse from the Ti:sapphire laser exciting the electrons in the GaAs sample into

their conductive state thereby increasing the reflectivity of the GaAs. As the electrons decay back to their insulator state the reflectivity begins to drop as there are less electrons in the conductive band. There are several processes by which the electrons will decay; carrier-carrier scattering, inter and intra-valley scattering, phonon scattering, and recombination of carriers. (Johnston, M, 2015)

Each of these processes occur over different periods in time. The majority of the electron decay takes place femtoseconds after the photoexcitation and lasts for a few picoseconds. This a result of carrier scattering either with themselves in an attempt to redistribute or with phonons (lattice vibrations). However, there are still some excess carriers. Which is the reason the graph in Fig 2 does not return to its equilibrium state. This final recombination of carriers takes place on the order of nanoseconds and is driven by either a radiative process or Auger recombination, which is the process of electron-hole recombination that either places another electron into the conductive band or pushes an electron hole further into the valence band. (Johnston, M, 2015)

4.2 Discharging Experiment

Previously, the ultrafast laser-trigger microwave emission experiments with YBCO showed that, when a persistent current is induced on the thin film ring and illuminated by a pulsed laser, the discharged current produced electromagnetic radiation. (Bullard, T J, et al., 2019) The bandwidth of the horn antenna used for detection of this microwave radiation limited the detection to a range of 5-18 GHz. (Bullard, T J, et al., 2019). It should be noted that the Ti:Sapphire laser used in the microwave study was amplified and implemented a pulse picker. A pulse picker is a device that allows for a single pulse from a pulse train to be selected and used. The pulse picker along with the amplifier allows for a single 1 mJ pulse to strike the charged YBCO ring. A single pulse from the amplified laser was shown to discharge the entirety of the

persistent current stored in the YBCO ring. The ultrafast Ti:Sapphire laser used in the experimental work reported here did not utilize a pulse picker and was not amplified, providing approximately 1-9.4 nJ per pulse. Due to this incredible difference between the laser pulse energies, it is believed that the decay of the current as a function of time could be observed. Experiments were conducted in which the laser was varied either in incident power or wavelength to determine if the decay rates of the persistent current were a function of laser fluence and/or the number of incident photons.

To determine the change in current as a function of time, a Hall probe was used to measure the magnetic field produced by the persistent current contained in the YBCO ring. When magnetic fields are orthogonal to a conductor with a current, there is a charge build up on one side or the other, depending on the direction of the B-field, due to the Lorenz force. The charge build up causes a change in potential across the conductor and that change in potential is what the Hall probe measures. The current in the ring is determined by the measured magnetic field by using the Biot-Savart law (Eqn. 4.1).

$$d\vec{B} = \frac{\mu_0 \vec{I} d\vec{L} \times \hat{r}}{4\pi r^2} \tag{4.1}$$

Where **B** is the Magnetic field, μ_0 is the magnetic permeability of free space, $\vec{I}$ is the current, $\vec{L}$ is the length of the conductor carrying the current, and r is the distance away from the conductor. The ring in use is considered an annulus, with an inner radius of (6 mm) and an outer diameter of (9 mm) and 200 nm thick. An image of the YBCO ring used is in Figure 4-3. The thickness of the sample was not used in the calculation, as it is negligible when compared to the track width of the sample. The sapphire substrate thickness is 1 mm, and all of the current calculations assumed the hall probe was 1 mm away from the center of the ring.

The superconducting ring's substrate was placed atop a copper pipe with an inner diameter of 5/16" with the diameter of the Hall probe being 1/4". The Copper tube was placed in a piece high density polyurethane which also had an opening wide enough for the Hall probe to fit into. The

Figure 4-3. Image of the YBCO ring while in the LN2 bath with the laser incident.

high density polyurethane with the hall probe inside was then placed into a Styrofoam bowl. With the ring in place on top of the copper tube and held in position with vacuum grease, the liquid nitrogen was added until the ring was fully submerged. The bowl was filled with liquid nitrogen to a marked point and extra LN2 was added during the experiment to ensure the volume of LN2 the laser had to pass through before hitting the YBCO was consistent (Figure 4-3) and Figure 4-4 is a diagram of how the laser is incident on the YBCO ring in the LN2 bath.

4.2.1 Laser Power Dependence on Discharging

The YBCO ring was initially charged to its maximum possible current density by using a neodymium magnet. The magnet was placed close enough to the ring to overpower the screening currents in the superconductor. When magnetic flux is allowed to pass through a superconductor

while in the superconductive state, a persistent current is placed on the ring. The magnitude of the current is directly related to the amount of discharged magnetic flux, the greater the discharged flux the greater the current. The persistent current eventually reaches a maximum which is determined by the amount of superconducting electrons available in the material. Experiments were also conducted where the ring was only partially charged. The partial charging was accomplished by using the ultrafast laser to charge the ring, which will be discussed in greater detail in the description of the charging experiment. When a persistent current is induced on the ring, there is a natural drop in current, without applying the laser, which exponentially decays to an asymptote over time. (Figure 4-5)
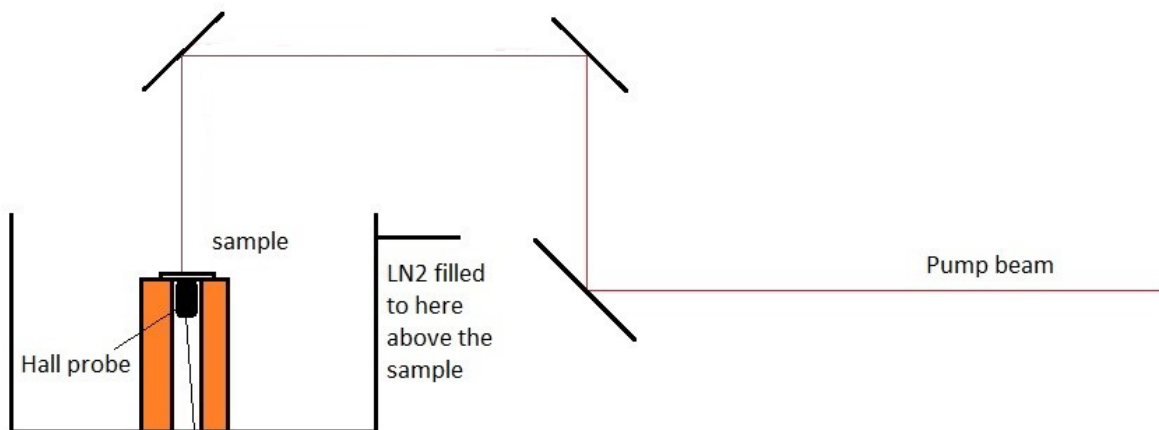

Figure 4-4. Diagram of the charging/discharging experiment. The YBCO sample is sitting on a hollowed out copper rod with a Hall probe positioned inside and directly beneath the sample.

The laser was focused onto the sample before the LN2 was added. It was noted in the microwave experiment and in these experiments, that a tightly focused laser will not discharge the current as effectively as one that is roughly the size of the track width. The LN2 was used to defocus the laser before illuminating the YBCO ring. The index of refraction for LN2 at its boiling point is approximately 1.198 for 800 nm. (Jacobsen, R, 1973) The increase in the index of refraction changing from air (n=1) to LN2 causes the focal length of the lens to become shorter

causing the beam to focus before it reaches the YBCO sample. The graph in Figure 4-6 demonstrates how the level of LN2 can affect the rates at which the current is discharged by the pulsed laser.
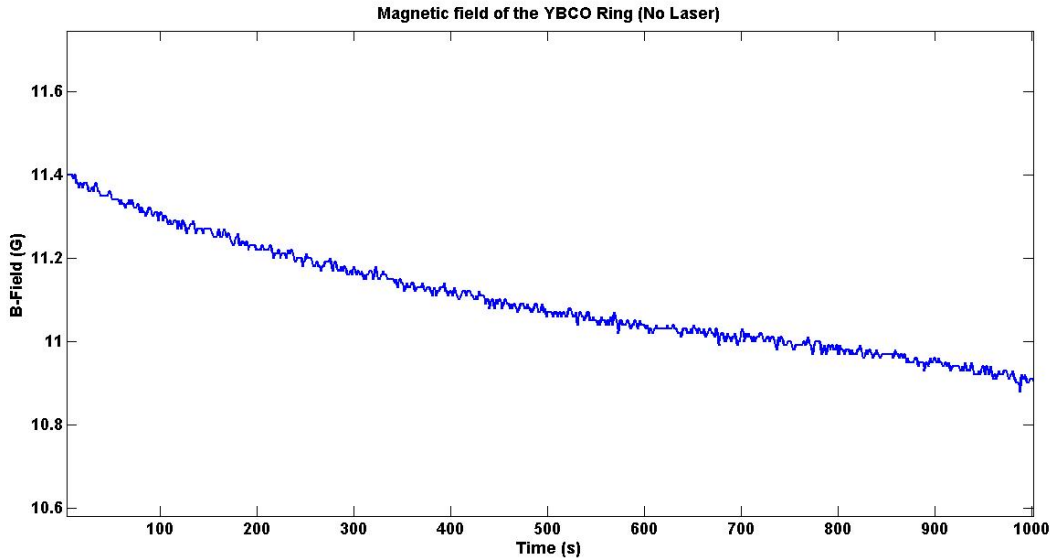

Figure 4-5. Graph showing how the B-field created from the current on the YBCO ring naturally decays over time after the maximum current is placed on it.

The average pump laser powers ranged from 50 mW to 750 mW. The average power was measured directly above the LN2. Various lengths of discharge time were also studied, ranging from 5 minutes to an hour of exposure to the ultrafast laser.

4.2.2 Wavelength Dependence

A study with varying different photon energies was also conducted. It was an effort to determine if the number of photons incident on the YBCO sample effected the discharge rate as well as laser fluence. The different wavelengths that were used all had the same average power, meaning that a shorter wavelength (higher energy) pulse requires less photons than a longer wavelength pulse to have the same average power. It was thought that photons in each laser pulse were interacting with the Cooper pairs which form the basis of the persistent current. If more photons are incident on the YBCO ring then the faster the discharge rates would be. The

31

Coherent Chameleon II Ti:Sapphire laser (with a central wavelength of 800 nm) is capable of being tuned to wavelengths ranging from 700 nm to 1000 nm.
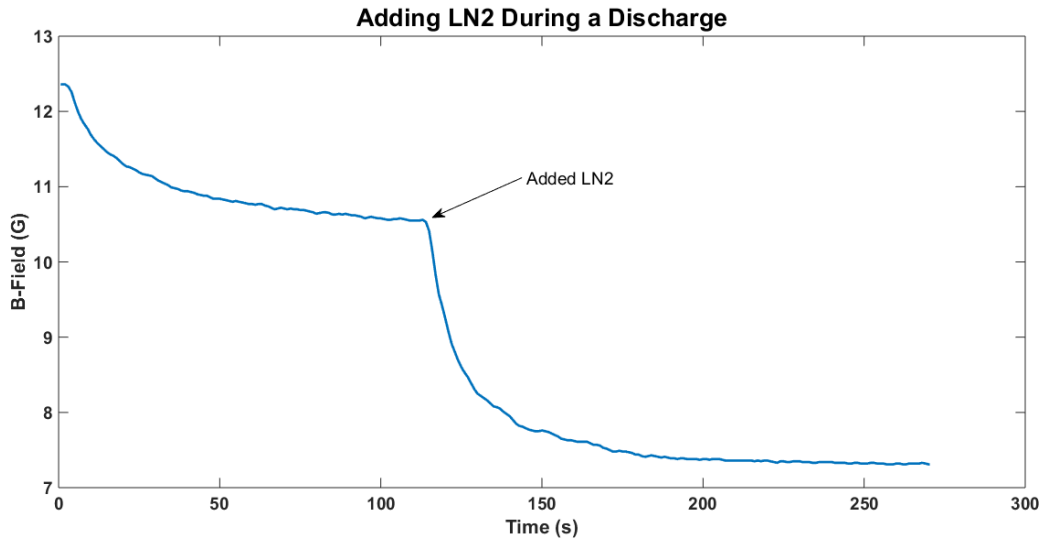

Figure 4-6. With the laser incident on a fully "charged" YBCO sample it was noted that varying the level of LN2 would drastically reduce the rate at which the current was discharged. Then adding LN2 caused the beam to defocus and continue discharging the current.

In addition to the tunable wavelengths offered by the Chameleon laser, a BBO (Barium Borate) crystal, often referred to as a doubling crystal, was used to convert the 800 nm light into 400 nm. A BBO crystal has a non-linear susceptibility, which leads to a second-order harmonic generation effect. The second order harmonic results in the combination of two photons to produce a third and when a laser is providing the photons only a single frequency is available, therefore, $\omega \rightarrow 2\omega$. (Fan, Y., 1989) The ultrafast laser needs to be tightly focused on the BBO crystal to work efficiently. Even then, the highest conversion efficiency that could be attained was 15%. The rest of the energy heats the crystal which effects the lattice structure enough to interrupt the two photon process. The maximum average power available at 400 nm was 109 mW.

4.3 Charging Experiment

Inducing a supercurrent on the YBCO ring was accomplished by either overpowering the screening current (the Meissner Effect) with the magnetic field from a magnet (approximately 40 Gauss), or by placing a weaker magnetic field near the ring (15 Gauss) and illuminating the sample with the Ultrafast laser. In the microwave emission study, the YBCO ring was initially charged by a single 150 fs pulse from the amplified laser while in the presence of a magnetic field. Similar to the discharging, a single pulse was able to induce the maximum possible current on the ring. It was believed that the increase in current as a function of time could also be observed.

Both methods of charging are believed to be due to the same process, trapping magnetic flux within the superconductor. When a superconductor is above its critical temperature, magnetic field lines can pass through the material freely. When a superconductor is cooled below its critical temperature while in the presence of a magnetic field, the superconductor dispels all magnetic field lines that exist within to become a "perfect" diamagnet. The trapped flux is then converted into a supercurrent.

4.3.1 Magnetic Charging

Using a magnet to overpower the screening currents is a result of the penetration depth of the superconductor. Even though a superconductor is a perfect diamagnet, some field lines still make it into the material. This effect is far more noticeable in a thin film than in a bulk material because the penetration depth of a magnetic field exponentially decays inside the material. To inspect how effectively a magnetic field induces a supercurrent on the YBCO ring, a neodymium magnet was attached to a micrometer and placed near the Styrofoam bowl. The YBCO ring was

placed on the copper cold finger with the Hall probe present and the bowl was filled with LN2. The magnet was moved into varied locations where the Hall probe would measure the magnetic field. The magnet was then removed and the measurement from the Hall probe would only measure the magnetic field from the induced current on the ring.

4.3.2 Laser Charging

Inducing a current on the YBCO ring via excitation by ultrafast laser is believed to be tied to the aforementioned process. The laser weakens the screening currents which allows the field lines to penetrate through the superconductor. The neodymium magnet was placed next to the Styrofoam bowl at a location where the Hall probe measured a field strength of 15 G. The same laser powers were used as the discharging experiment as well as the same exposure times. If the YBCO ring charges and discharges by the same superconductive mechanism for each approach, comparison of the discharge rates would provide confirmation.

4.4 Time Domain THz Emission Experiment

The final experiment was to determine if THz radiation was being emitted and it was, could it be detected by discharging the current in the YBCO ring. A time domain system was built and tested using p-InAs as the THz emission source material, which can create THz light via the Photo-Dember effect, to ensure that it was capable of THz time-domain measurements. The original set up for the time domain system used a cryostat as the mount for the p-InAs. All YBCO measurements were originally planned to use a cryostat, but it was discovered that the ring would not hold a current when placed in the cryostat. The possible reasons will be discussed in the results section.
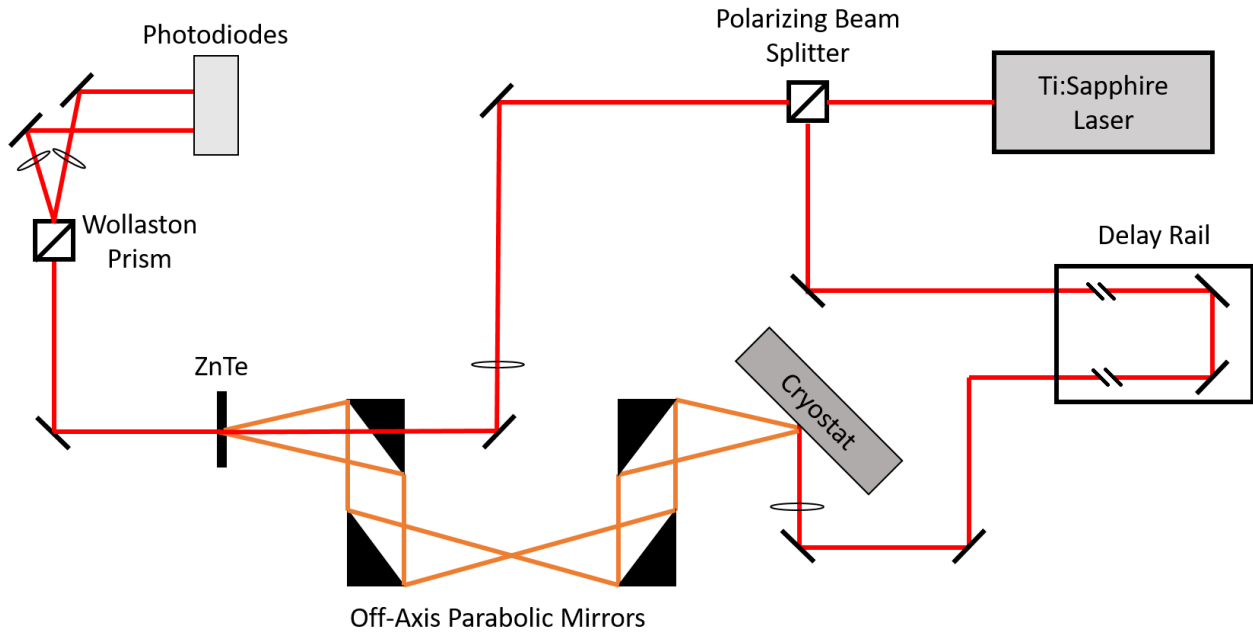
Figure 4-7. THz Time domain emission spectroscopy experimental setup. (Label the p-InAs)

The time domain experiment closely resembles the pump probe measurements. The ultrafast Ti:Sapphire laser is split into horizontal and vertical polarizations at the cube beam splitter. The pump beam (vertically polarized) is sent to the delay rail, optically chopped at 2 kHz, and then focused onto the p-InAs, Figure 4-7. The pump beam is focused with an adjustable lens and is blocked by a 500 μm thick wafer of high resistivity silicon after illuminating the p-InAs. The pump beam needs to be blocked after reflecting off the p-doped InAs, because it will overload the photodiodes and it also has enough fluence to damage the ZnTe crystal. The THz light produced by the p-InAs is horizontally polarized, the polarization is due to the orientation of the
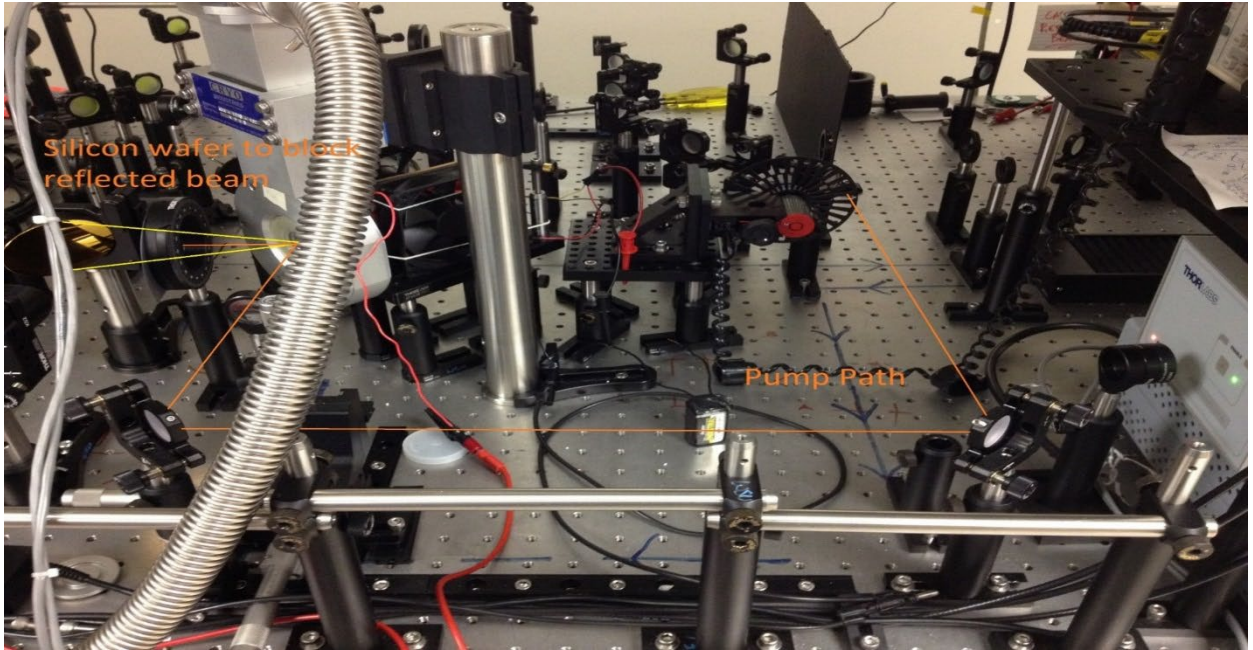
Figure 4-8. Picture of the pump beam path though the focusing lens onto the p-InAs.
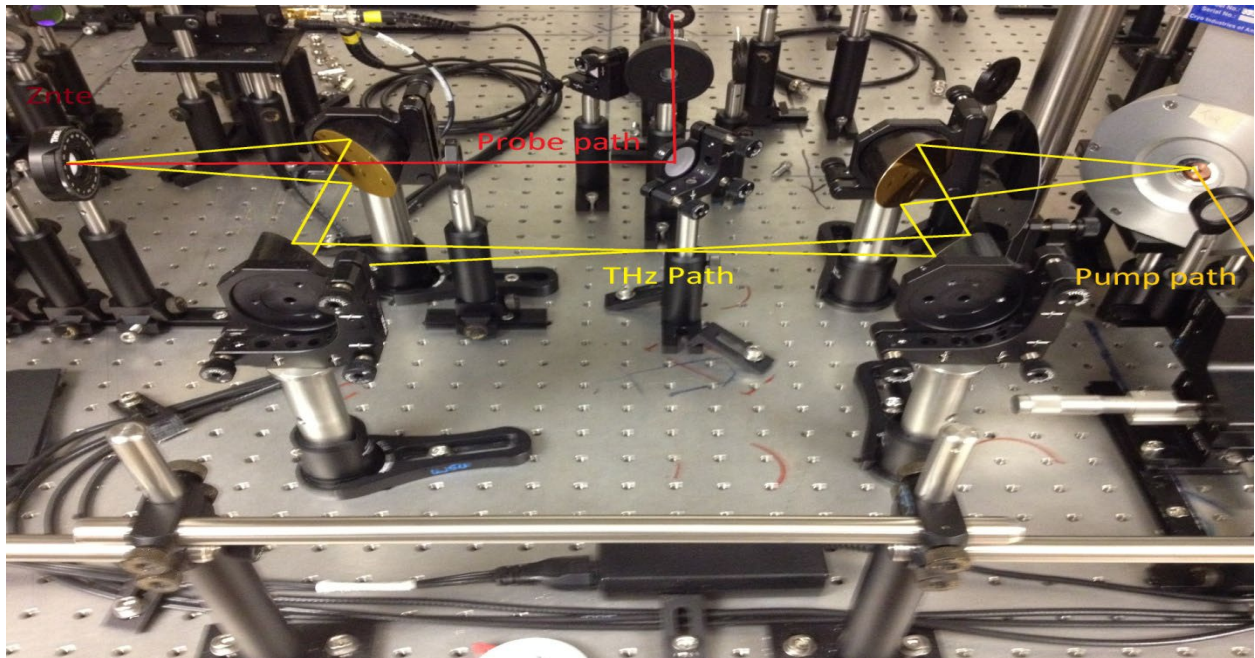

Figure 4-9. Picture of the THz path through the off-axis parabolic mirrors and how it meets up with the probe beam on the ZnTe

p-InAs and the laser, and is able to pass through the silicon wafer which exhibits 70%

transmission at THz frequencies. The THz light is collimated and focused onto a Zinc Telluride

(ZnTe) crystal by off-axis parabolic mirrors, Figure 4-8.

The probe beam (horizontally polarized) is folded several times as it must travel the same

optical path distance to the ZnTe crystal as the pump beam path and the THz light path

combined. In the microwave emission work, horn antennas were used to detect the radiation

from the ring. A horn antenna can produce and detect a small bandwidth of radiation due to its

size. THz light can still be detected by use of an electro-optic detection scheme using a crystal

such as ZnTe. When THz radiation is focused onto the ZnTe it becomes birefringent. The change

in index of refraction is related to frequency of the pulse ω, thickness if the ZnTe crystal L, the

speed of light c, the unperturbed index of refraction n_0, EO coefficient r, and energy of the THz

pulse E_{THz}, Equation 4.2.

$$\Delta n = \frac{\omega L}{c} n_0^3 r E_{THz} \qquad (4.2)$$

The change in in the index of refraction is measured by placing a quarter wave plate after the

ZnTe. In the absence of THz radiation the quarter wave plate is rotated until the probe beam is

circularly polarized. When the ZnTe index of refraction is altered by the THz radiation the

polarization of the probe beam after quarter wave plate is now elliptical. The horizontal and

vertical components of the polarization are then separated by a Wollaston prism and the

difference is detected by a pair of amplified photodiodes.

Differential detection and a lock-in amplifier are used to measure the intensity of the THz

pulse at a point in time. When there is no THz pulse present the both horizontal and vertical

components are of equal intensity, circularly polarized, the differential result is zero. When the

probe beam is elliptically polarized there is a non-zero result. The difference in intensities in the amplified photodiodes is sent to the lock-in amplifier. Equations 4.3-4.5 describe the changes in intensity of the s-polarized and p-polarized components of the probe beam and how it is proportional to the intensity of the THz pulse.

$$I_s = \frac{1}{2}E_{THz}(1 + \Delta n) \tag{4.3}$$

$$I_p = \frac{1}{2}E_{THz}(1 - \Delta n) \tag{4.4}$$

$$I_s - I_p = i_0 \Delta n = \frac{\omega L}{c}n_0^3 r E_{THz} \propto E_{THz} \tag{4.5}$$

The differential signal is sent to a lock-in amplifier. The THz pulse is modulated by an optical chopper operating at 2 kHz which chops the pump beam after the delay rail allowing for lock-in detection. The lock-in amplifier only detects signals at the frequency of the optical chopper reducing SNR and potentially allowing for signal resolution in nanovolts.

Optimization of the time domain system is crucial to the sensitivity of the detection. EO detection relies upon the precision of the alignment of the optical elements and the timing of the pump and probe paths. P-InAs is highly reflective and was used to verify the proper alignment of the off-axis parabolic mirrors. The pump beam was allowed to travel from the p-InAs to the ZnTe crystal to align the pump and probe beams. Viewing the ZnTe through the IR viewer, the off-axis parabolic mirrors were adjusted to ensure that not only were the pump and probe beams overlapped on the ZnTe, but that they were parallel as they approached the ZnTe.
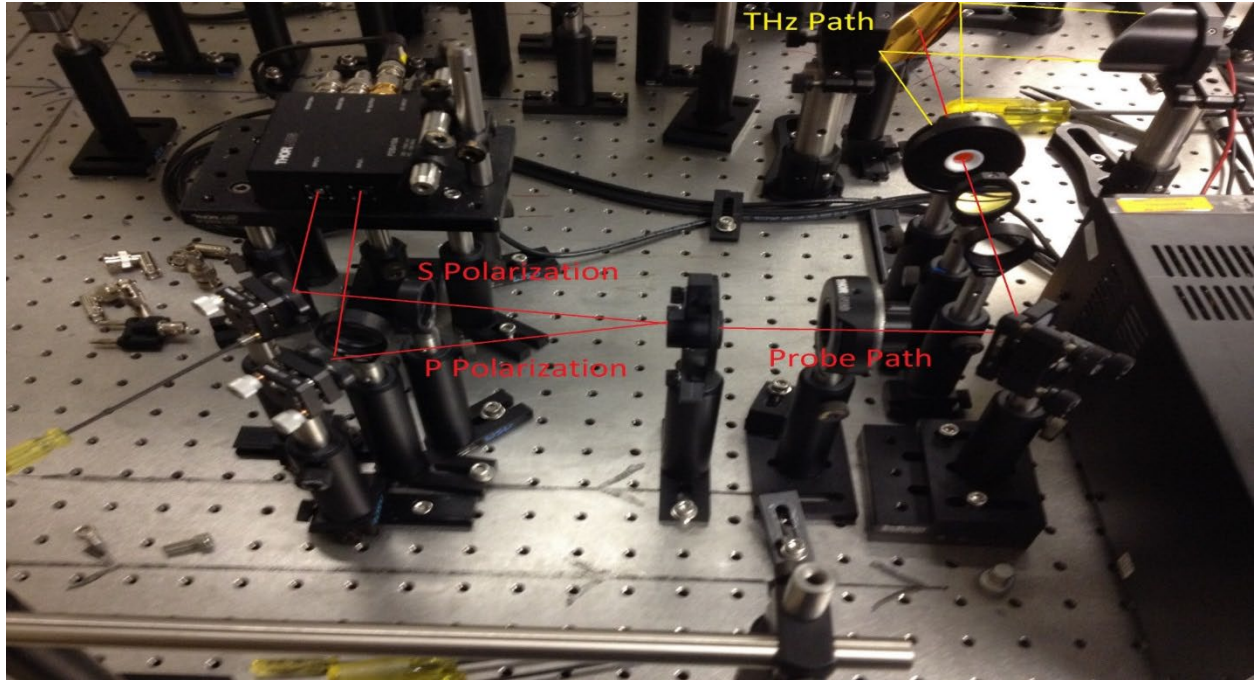
Figure 4-10. The probe beam is elliptically polarized by a $\frac{\lambda}{4}$ wave plate and split into its vertical and horizontal components by a Wollaston prism. Then the split polarizations are sent to photodiodes where a lockin amplifier subtracts the signal from each other.

Additional optimization techniques include adjusting the delay rail so the probe pulse is matched up to the peak of the THz radiation pulse and adjusting various optical components to maximize the signal. The optical components that seemed to matter the most were the pump beam focusing lens, the location and orientation of the ZnTe crystal, and slight adjustments in the off-axis parabolic mirrors. The pump beam needs to be focused down onto the p-InAs which also needs to be the location of the focal point of the off-axis parabolic mirror. This helps to maximize the amount of THz light that is collected by the first parabolic mirror. The ZnTe also must be oriented in the proper direction, which is $< 1\,1\,0 >$. If the polarization of the THz radiation or the probe beam is not oriented along the lattice of the crystal the index of refraction will not have the maximum amount of change thereby reducing the signal and efficiency of the system.

4.5 YBCO Time Domain Experiment

The YBCO time domain experiment was attempted using the Styrofoam bowl in which the charging and discharging experiments were completed. The main complication was that the THz radiation would have to pass through the LN2 before reaching the parabolic mirrors. The index of refraction of LN2 at THz frequencies is about the same as the 800 nm light, 1.2. With the amount of LN2 present in the cooling bowl, the additional path length of the THz pulse would result in the pulse no longer being detectable using the delay rail. In an effort to minimize the amount of LN2 between the YBCO ring and the edge of the bowl, sheets of Styrofoam were placed in the bowl to displace the LN2. Fortunately, Styrofoam is nearly invisible to THz radiation (Figure 4-13). The Styrofoam attenuates the signal about as much as the silicon wafer did.
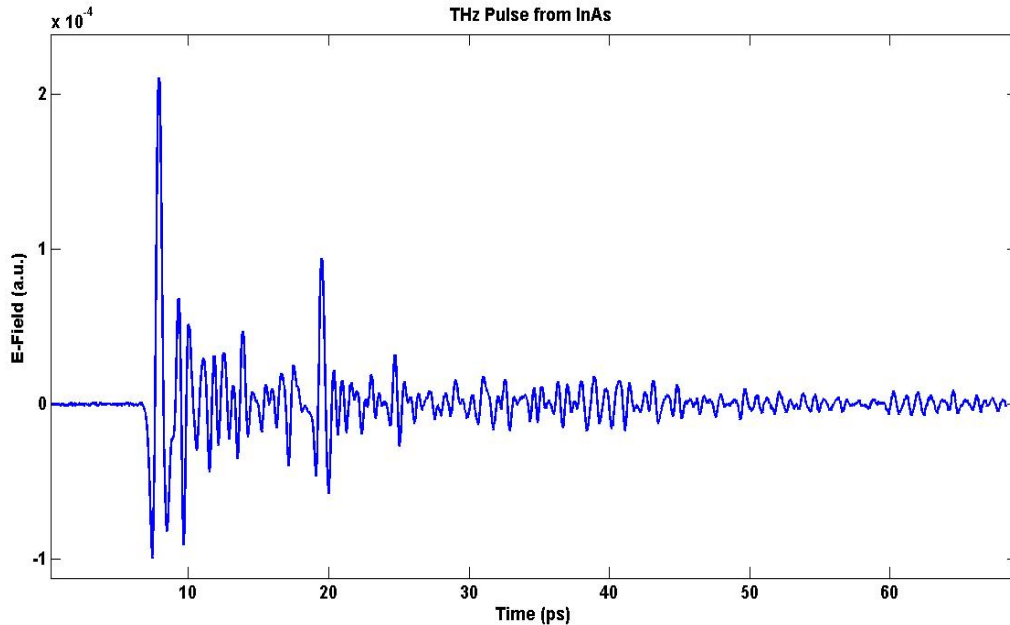

Figure 4-11. Plot of the optimized THz pulse generated from the p-doped InAs as a function of time. The second peak is from the etalon reflection in the silicon wafer and can be clearly seen at the 20 ps mark.
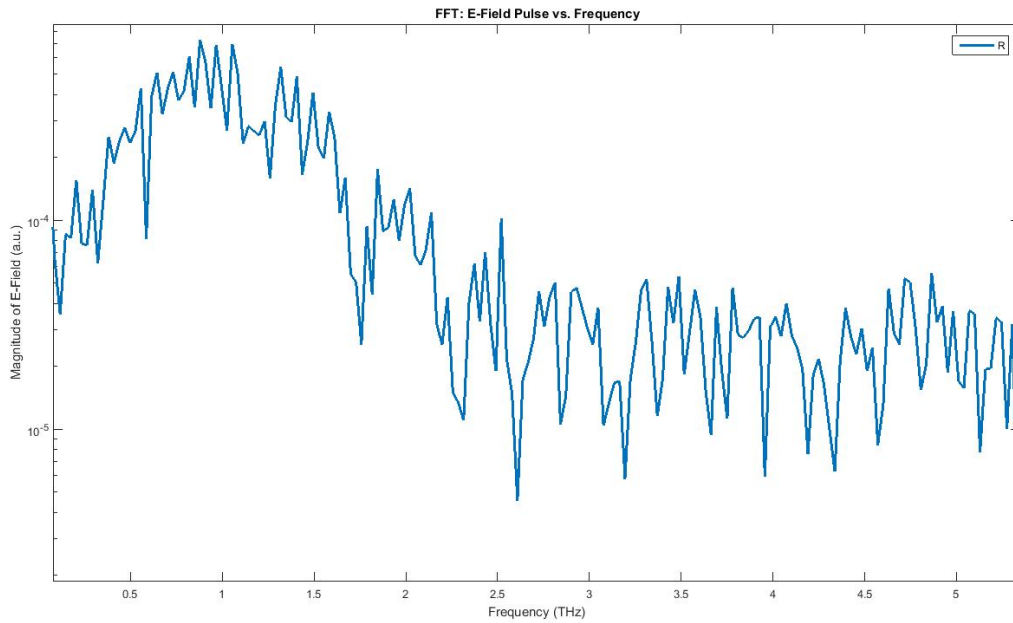
Figure 4-12. The spectrum of the THz pulse produced by the Photo-Dember Effect from the p-doped InAs.
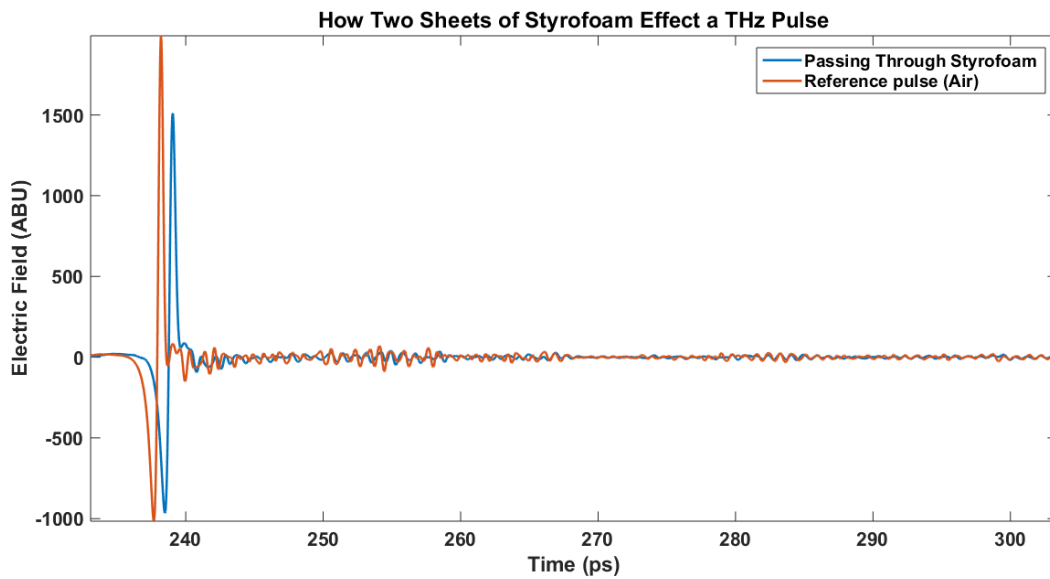

Figure 4-13. THz pulse interacting with sheets of Styrofoam (Data taken from Teraview system)

The same pump powers were tested that were used in the charging and discharging experiment, they are listed in table 5-1. The time domain experiment was also ran with and without a magnet in place. It was noticed during the microwave experiments that while using the

41

ultrafast laser pulse to charge the YBCO ring a signal was also received by the horn antenna.

Therefore, a signal should still be detected while the ring is being charged by the laser.

5. Results

The first experiment attempted to detect THz radiation from the YBCO while the ring was within the cryostat. The ring was placed in the cryostat in the same location and in the same manner as the p-doped InAs. This experiment yielded no THz signal. In an effort to diagnose why we were not detecting THz radiation in the Time Domain experiment several other experiments were designed. The experiments discussed in the rest of this section were conducted to probe electron response and relaxtion times for YBCO, determine how to effectively induce a persistent current on YBCO, and how that persistent current is discharged.

5.1 Pump-Probe Measurements

To determine if the YBCO ring was experiencing a picosecond electron response a pump-probe measurement experiment was prformed. The YBCO ring was placed in the cryostat on a copper cold finger and held in place with vacuum grease. The experiment was carried out twice, with LN2 and without. In both experiments the pulsed laser was passed through a quartz window on the cryostat to reach the YBCO thin film. Quartz has a low reflectance (0.0066 with P-polarization at 45 degrees) (Malitson, I. H., 1965) and low absorption at 800 nm and can structually handle the low pressure of the vacuum. The only difference between the two experiments was adding LN2 to the cryostat.

The YBCO thin film had shown a photoresponse to the pulsed laser when LN2 was added to the cryostat. (Figure 5-1) When in its superconductive state YBCO has a partial energy gap therefore, a pump-probe response was anticipated. The band gap for YBCO is on the order of milli-electron volts which is the amount of energy needed to break a cooper pair (ZHAO, G. L., and D. BAGAYOKO., 2012).
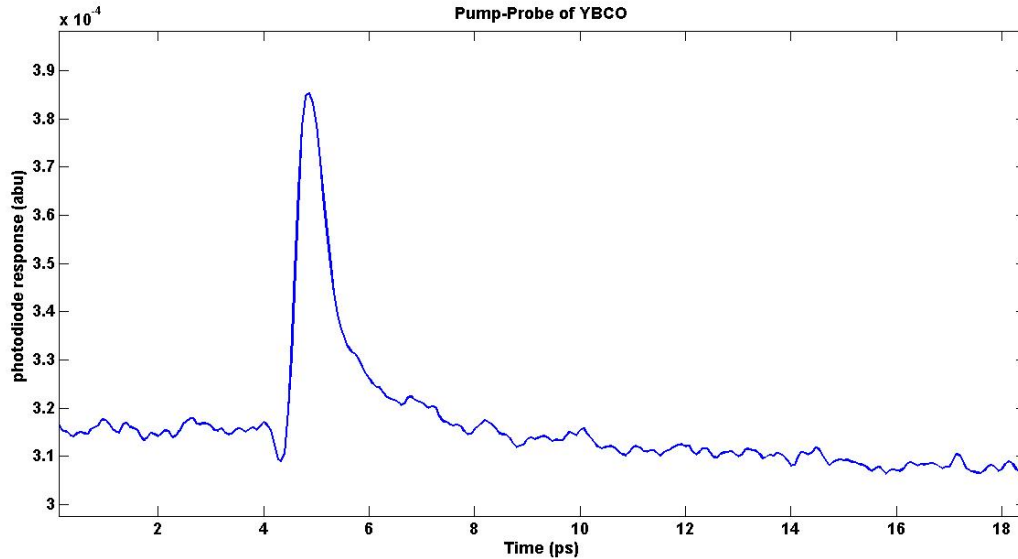
Figure 5-1. Photoresponse of YBCO when using LN2 to cool the cryostat.

There was no photoresponse to the pulsed laser when the YBCO ring was at room temperature (figure 5-2), 296K. Which was expected as YBCO is not a semiconductor, but an insulator. The shown photoresponse does not indicate that the YBCO thin film was in its superconductive state. As previously discussed YBCO has a psuedogap phase in which the electrons can move into the conductive band while the material is not in its superconductive state. For YBCO, the pseudogap phase typically exists when the crystal contains less oxygen when compared to optimally doped YBCO. As a result, under doped YBCO has a lower crtial temperature than optimally doped YBCO (Segre, Gino P., 2001)

An axial Hall probe was installed into the cryostat to determine if a persistent current could be induced while the YBCO thin film was in the cryostat. The Hall probe was located directly behind the YBCO substrate and was wired into the existing wiring n the cryostat. While the Hall probe could detect a magnetic field from a source outside of the cryostat it could not detect a magnetic field from the YBCO thin film.
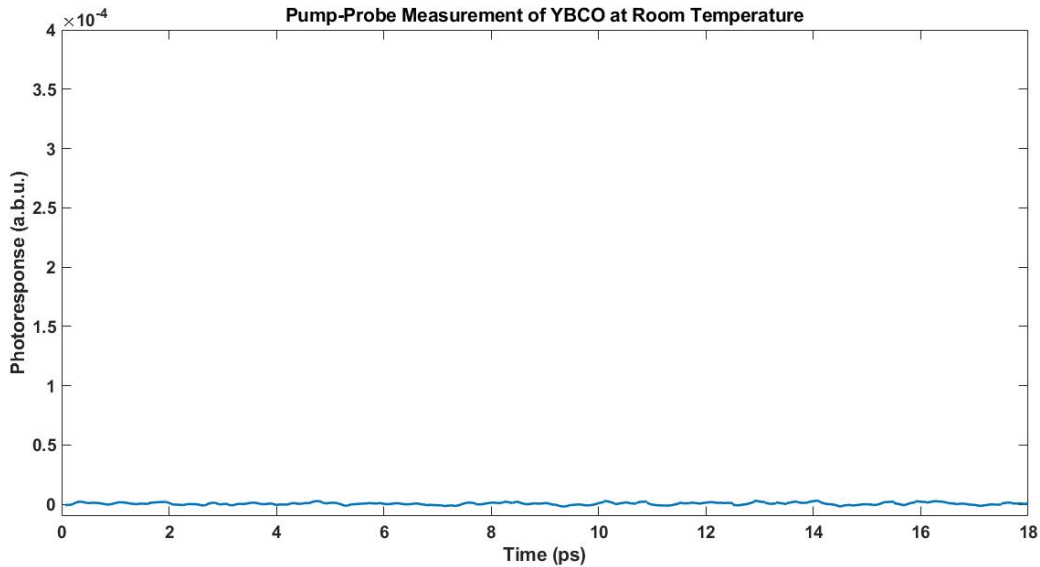
Figure 5-2. YBCO optical response to a pulsed laser at room temperature.

It is our belief that the cryostat could not cool down the thin film YBCO below its critical temperature. Even though a photoresponse was observed, a persistent current could not be induced. When the thin film YBCO was placed in a liquid nitrogen bath a persistent current was induced. A temperature gradient mostly liked formed from the conduction cooling crossing over multiple interfaces. Coupled with a lowered critical temperature from being under doped could have lead to the YBCO not reaching its superconducting phase.

5.2 Charging the YBCO Thin Film

In the experiments dicussed in this paper a "charge" was induced on the YBCO thin film and then discharged. The term "charging", will refer to the persistent current induced on the YBCO annulus. There were two methods used to charge the thin film annulus. For the first method the YBCO thin film was placed in a magnetic field large enough to take advantage of the magnetic penetration depth (50 Gauss). For the second, the YBCO thin film was placed in a significantly smaller magnetic field (20 Gauss) but with a Ti:Sapphire laser incident on it.

5.2.1 Magnetic Charging

There were two methods used to induce a persistent current in the YBCO thin film by only using a magnetic field. If the material is in a magnetic field when it switches over to its superconducting state a current will form in the material. Superconductors will dispell all magnetic field lines existing within them because it is energetically favorable to do so. Since flux must be conserved it is converted into a current . Since there is zero resistance in a superconductor that current is persistent.

The second method requires the use of a thin film to take advantage of the magnetic penetration depth. Even though a superconductor is a diamagnet some field lines will still penetrate the material. If the field lines completely penetrate through the material and the source of the magnetic field is removed the trapped flux will also be converted to curent.

The decay of the magnetic field within the material is exponential with distance and the penetration depth is tyically on the order of hundreds of namometers for a type II superconductor. The London penetration depth for YBCO at 77 K is 185 nm (Prozorv, R, et al., 2000) Figure 5-3 displays how the strength of the magnetic field placed on the ring changes the induced current on the ring.

Rearranging Equation 3.5, where B is the magnetic field from the current in the super conductor and B_0 is the applied magnetic field, and λ_L is the London penetration depth

$$x = -\ln\left(\frac{B}{B_0}\right)\lambda_L(T) \tag{5.1}$$

Equation 5.1 yields the thickness of the thin film. The applied magnetic field is treated as the magnetic field which is at the surface of the thin film. The magnetic field resulting from the

induced persistent current is treated as the magnetic field that has penetrated through the thin film. The current must produce the same magnetic field which has completely penetrated the superconductor. The anticipated thickness of the thin film is 200 nm. Figure 5-4 shows our calculated thickness of the film as a function of the applied magnetic field.
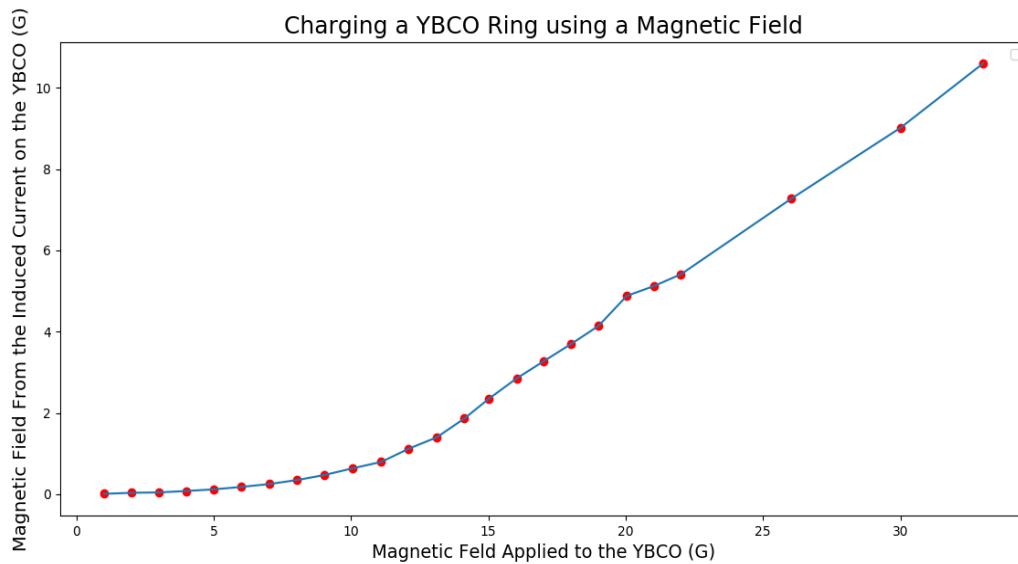

Figure 5-3. A graph which shows the applied B-field on the ring and the B-field from the persistent current induced by the applied B-field.

There was some difficulty in recording the measurements that were under 1 Gauss. Even though the axial Hall probe used to record the magnetic field data is rated for cryogenic temperatures the readings were very unstable. The boiling LN2 bath caused the probe wires to jostle, decreasing the accuracy of the magnetic field readings from $1\ G\ \pm 0.001$ to $1\ G\ \pm 0.2$. I believe this is the reason for the inaccuracies in the beginning of the graph. All of the measured values from the induced persistent current were under 1 Gauss if the applied magnetic field was under 10 Gauss.
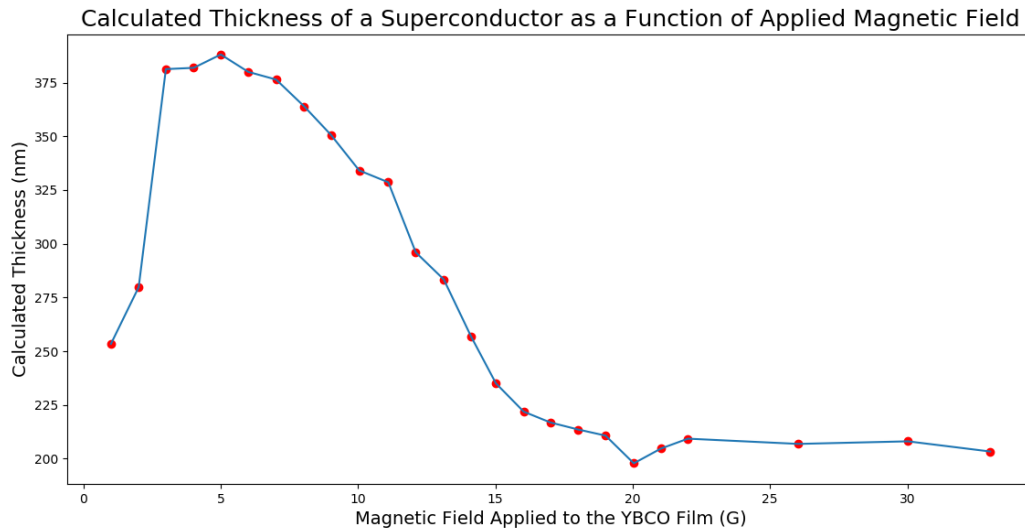
Figure 5-4. A graph using the applied magnetic field in comparison to the resulting persistent current to determine the thickness of the YBCO thin film.

5.2.2 Laser Charging

The second method of charging the YBCO thin film uses a pulsed laser. It was accomplished with the YBCO sample in the same configuration as the magnetic charging experiment. With the thin film in the presence of smaller magnetic field, 20 Gauss, a pulsed laser was directed to the sample's surface. From the previous experiment on magnetic charging, a 20 Gauss magnetic field can only induce 5.91 A of current, which generates a magnetic field of 4.88 G on the thin film. With the pulsed laser incident on the YBCO thin film a current builds up with an exponential decay which resembles the charging of an inductor. Equation (5.2) describes inductor charging where I_{max} is the maximum current passing through the inductor at $t = \infty$, R is the resistance in the circuit, and L is the inductance.

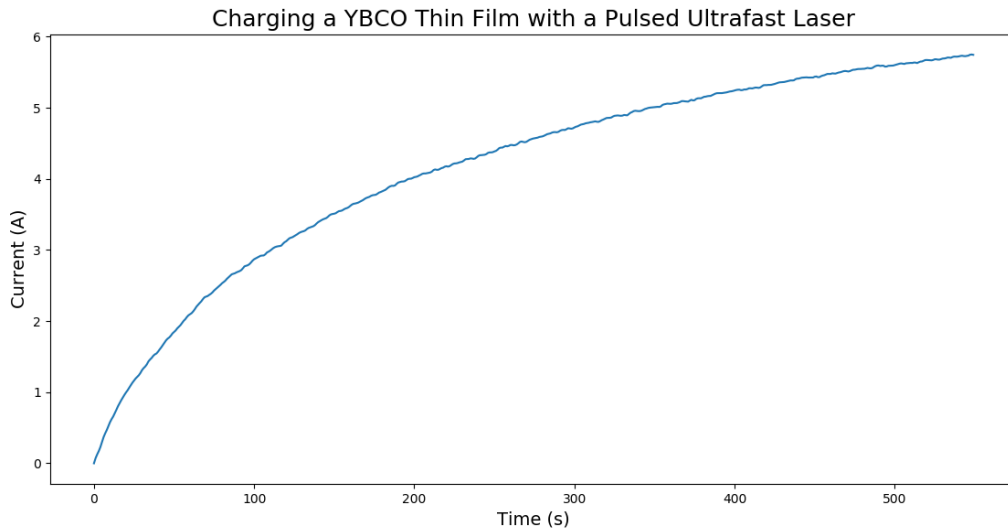$$I = I_{max}\left(1 - \exp\left(-\frac{tR}{L}\right)\right) \tag{5.2}$$

Figure 5-5. Charging the YBCO thin film with a 109 mW average power pulsed Ti:Sapphire laser with the sample in the presence of a 20 G magnetic field.
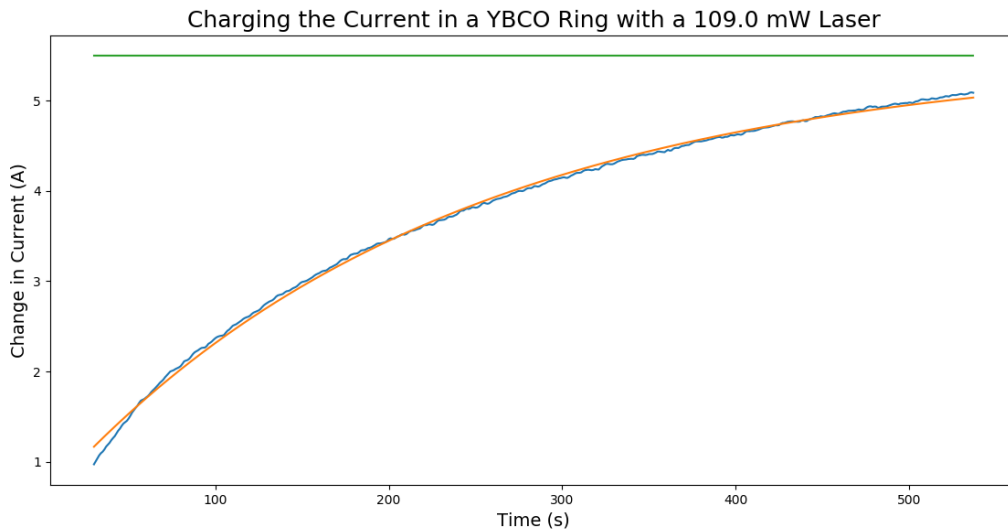

Figure 5-6. Charging the YBCO ring compared to a fit line equation $a * (1 - \exp(b * t)) + c$ where a = 4.94, b = -0.0044, c = 0.56. The green line represents the maximum possible current. The first 60 s of data were not used to determine the fit line due to some residual charging from the YBCO sample being in the presence of a magnetic field.

The laser charging experiments used various laser powers to determine if there was dependence on the charging time constant. Six different averaged laser powers were used to inspect any power dependencies on charging the YBCO thin film. Figure 5-7 shows there was not only a power dependence on the time constant, but also there was a maximum current that

could be induced on the YBCO thin film. If the laser power is increased, the magnitude of the time constant increases along with the maximum current that can be induced on the super conductor.

Charging the Current in a YBCO Ring with a 190.0 mW Laser
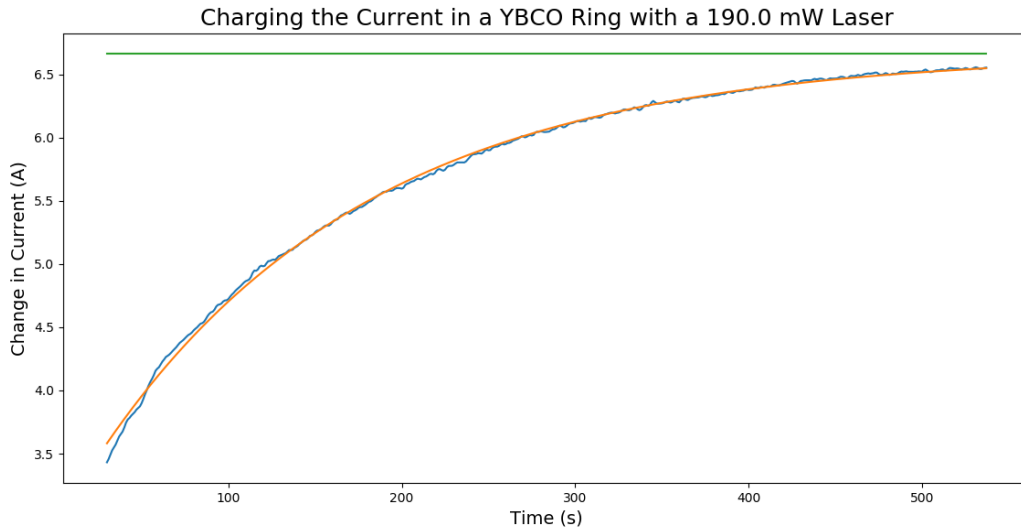
Figure 5-7. Charging the YBCO ring compared to a fit line equation using a 190 mW pulsed laser, where green is the asymptotic current, orange is the fit line, and blue is the data.

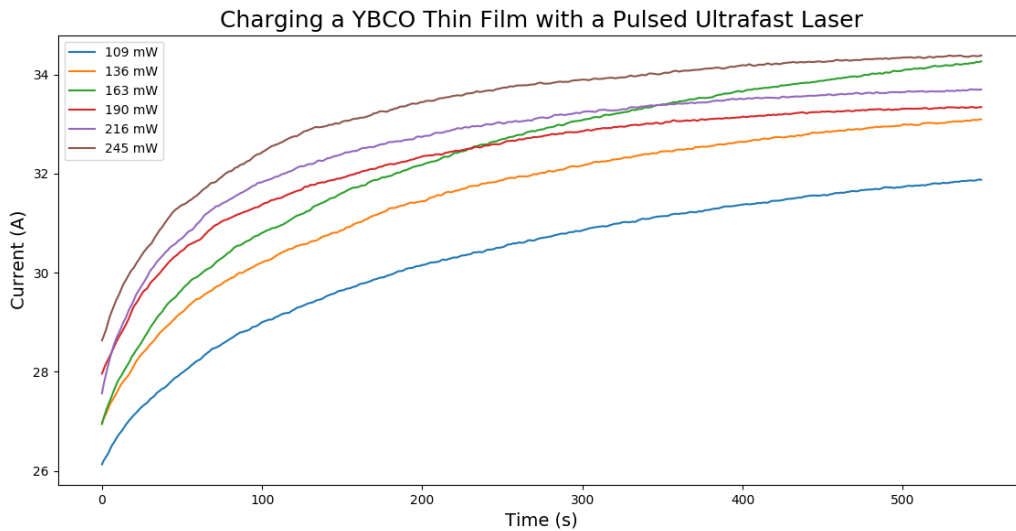Charging a YBCO Thin Film with a Pulsed Ultrafast Laser

Figure 5-8. Persistent current dependence on laser power. An increase in laser power shows an increase in charging rate and maximum attainable current.

Average Laser Power	Time Constant	Maximum Attainable Increase in Current
109 mW	-0.0044 s	5.50 A
136 mW	-0.0050 s	6.06 A
163 mW	-0.0045 s	7.93 A
190 mW	-0.0065 s	6.67 A
216 mW	-0.0074 s	6.92 A
245 mW	-0.0076 s	7.60 A

Table 5-1. Comparing differences in time constants and maximum change in persistent current due to changes in the average power of the Ti:Sapphire laser.

There is a correlation between average laser power and the maximum persistent current that is induced on the YBCO thin film. It appears as though the magnetic penetration depth of the thin film is increasing with laser power. An increase in magnetic penetration depth would allow for greater magnetic flux through the YBCO thin film. It has been shown that YBCO has an electron response to the Ti:Sapphire laser by breaking Cooper pairs. The electrons available are responsible for creating the screening currents, which attempt to cancel out the magnetic fields within the YBCO thin film. When the pulsed laser breaks Cooper pairs, the electrons that comprise them are no longer available to screen the applied magnetic field, which results in a larger current.

The rate at which the current builds in the YBCO thin film is proportional to the laser power. If there is an increase in average power, there is an increase in the number of photons per laser pulse. More photons correlate to an increase in the number of broken Cooper pairs allowing a greater amount of magnetic field lines to penetrate the material during each laser pulse resulting in an increased rate of charging.

The abnormal data from the 163 mW laser power test resulted from a LN2 level that was inconsistent with the other tests. Based on the shape of the graph there was an excess amount of LN2 in the bowl resulting in an increased laser spot size on the YBCO. A larger spot size allows

more electrons to be effected by each laser pulse resulting in an increased rate of charge. If the laser is focused on the thin film very little charging takes place. Consequently, this shows that pulsed laser is not locally heating the material above its critical temperature.

5.3 Laser Discharging

To generate THz radiation we must be able to deplete the current in the YBCO thin film. The rate at which the current changes will determine the strength of the electromagnetic radiation generated by the thin film. The laser discharging experiment was performed in the same manner as the laser charging experiment except with a longer duration, 20 minutes instead of 10 minutes.

The persistent current on the YBCO thin film decayed at an exponential rate when the Ti:Sappire laser was incident on it. The exponential decay in this experiment is similar to that of a discharging inductor. This was the expected result. It was assumed that since the YBCO ring charged like an inductor it should then discharge in the same fashion.

$$I(t) = I_0 \exp\left(-\frac{R}{L}\tau\right) \tag{5.3}$$

The averaged pulsed laser power used to deplete the ring determined the maximum persistent current the ring could have and the rate at which the ring discharged. The current asymptotically approached a minimum value which was determined by an exponential fit. Where a is the amount of current depleted, b is the time constant of the exponential, and c is an offset or in this case the asymptotic current the exponential approaches.

$$I(t) = a * \exp(b * t) + c \tag{5.4}$$

The decay of the persistent current was measured for 13 different laser powers on three separate occasions and averaged, Figure 5-9. The deviation between each of the measurements is

low at both the start and end of each data set when compared to the central portion. The laser power ultimately determines the amount of persistent current the thin film can sustain, but the variance in the rate of decay is most likely due to slight differences in the amount
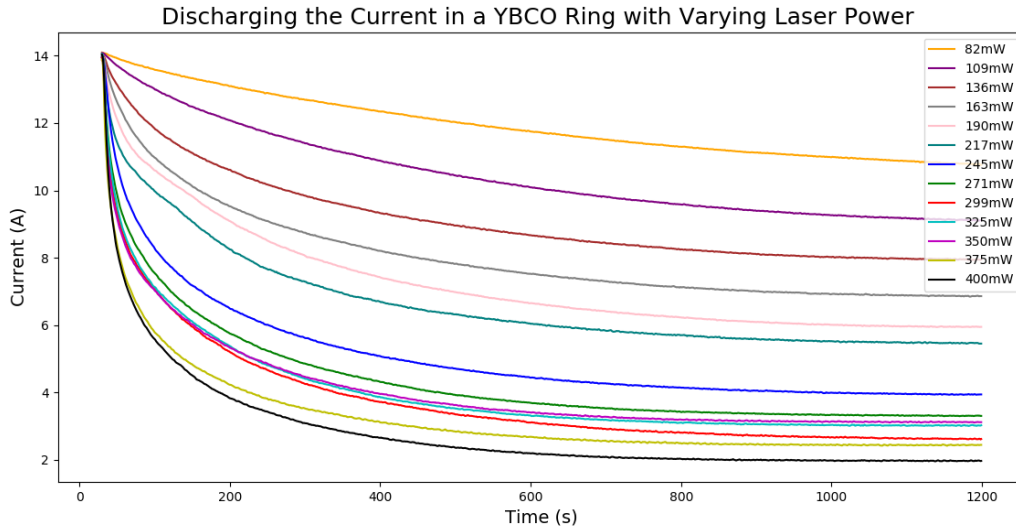

Figure 5-9. Decay of a persistent current from varying laser powers.

of LN2 used in the bath. The laser has to pass through LN2 before it arrives at the thin film. The change in index of refraction between air and the LN2 increases the focal length of the focusing lens. The amount of LN2 the beam passes through changes the spot size of the laser on the YBCO thin film. If the laser spot size is too small, the laser pulses will not be able to interact with enough electrons to either charge or discharge the current. The concentration of photons is too great and the area in which the laser is focused and becomes over saturated. If the spot size is too large, the concentration of photons is too low to effect enough electrons.
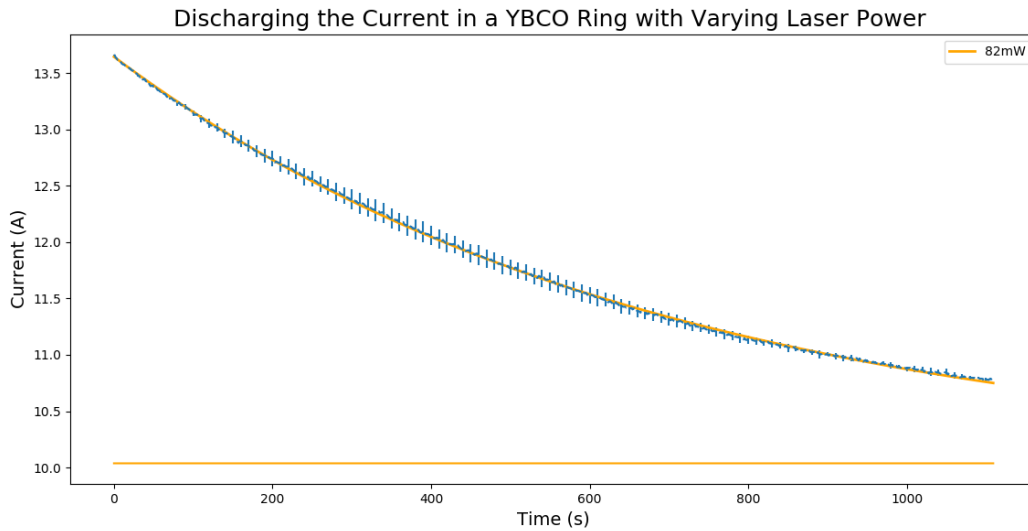
Figure 5-10. Persistent current decay using an 82 mW average laser power. In blue is the averaged data with standard deviation, in orange is the fitted data with the minimum current the data is approaching.
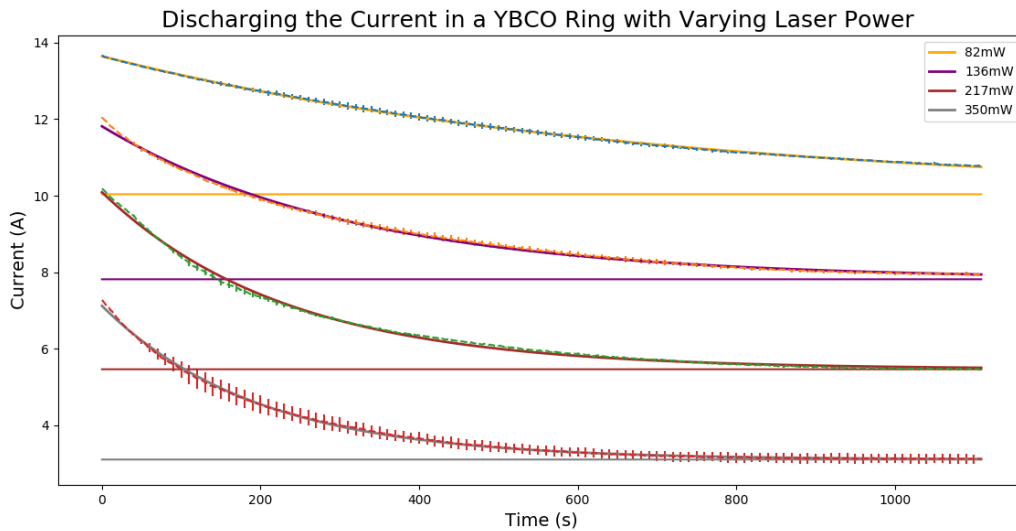

Figure 5-11. Four separate laser powers, 82 mW, 136 mW, 217 mW, 350 mW, with the first 60 s of data removed due to the natural discharge of the ring. The graph shows the laser power dependence on the decay rate and the asymptotic current.

It is believed the exponential fit applied to the asymptotic curve graph relates to the optical penetration depth of the 800 nm into the YBCO thin film. At 800 nm, the optical penetration depth of YBCO is 100 nm (Segre, Gino P., 2001). When more energy is added per pulse, it allows for a greater number of photons to penetrate the material. Since Cooper pairs only travel

on the copper oxide planes the 800 nm photons would need to penetrate the material in order to

reach the electrons existing on the copper oxide planes within the YBCO.

Laser Power	Time Constant	Maximum Current
82 mW	0.0015 s	10.04 A
109 mW	0.0023 s	8.73 A
136 mW	0.0031 s	7.81 A
163 mW	0.0035 s	6.78 A
190 mW	0.0037 s	5.86 A
217 mW	0.0043 s	5.46 A
245 mW	0.0044 s	3.94 A
271 mW	0.0048 s	3.29 A
299 mW	0.0046 s	2.63 A
325 mW	0.0053 s	3.01 A
350 mW	0.0051 s	3.10 A
375 mW	0.0054 s	2.43 A
400 mW	0.0057 s	1.97 A

Table 5-2. Time constants and asymptotic floor for each laser power level as determined by the fit lines.
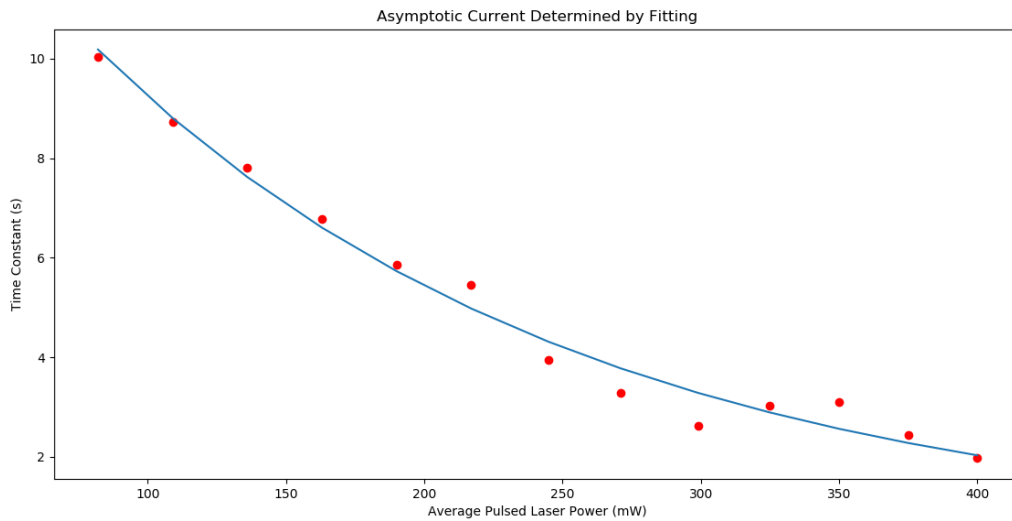

Figure 5-12. Graph of the asymptotic current for each of the separate power levels used to discharge the persistent current.

5.4 Wavelength Experiments

To determine if the power dependence is due to photon energy or number of photons a

wavelength experiment was performed. The Coherent Chameleon Ultra II Ti:Sapphire laser can

be tuned to provide pulses over a range of wavelengths, 700 nm – 1100 nm. The wavelengths

inspected for this experiment ranged from 750 nm to 850 nm in 25 nm steps and were kept at the

same average power. When each wavelength has the same average power, there is a decrease in the number of photons per pulse as the wavelength decreases because there is more energy per photon.
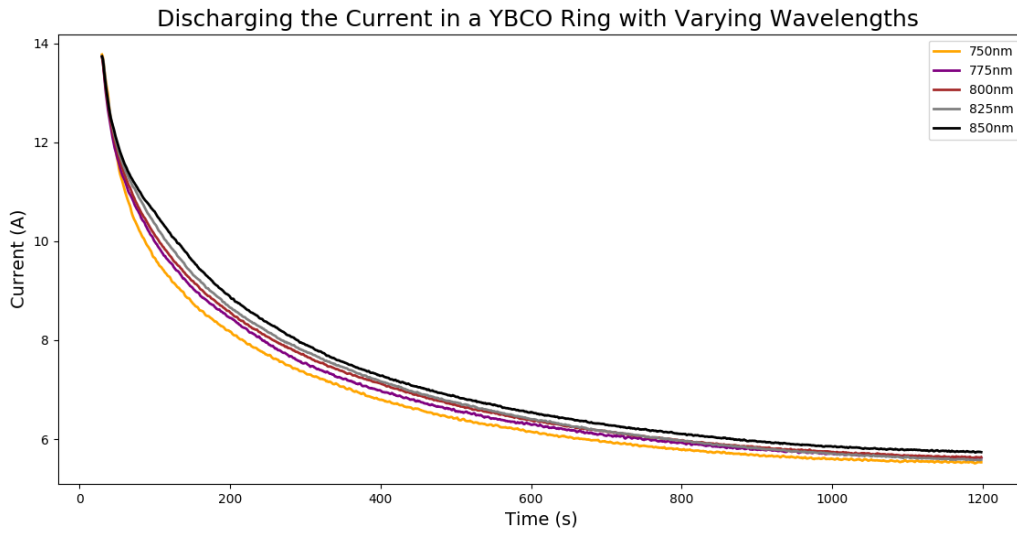

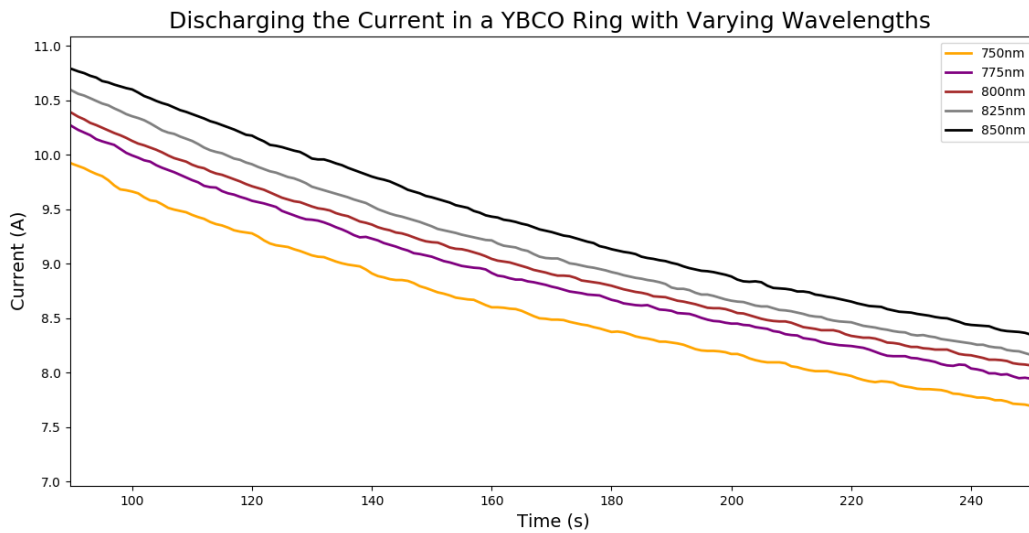Figure 5-13. Discharging the YBCO thin film using various wavelengths.

Figure 5-14. Close up of figure 5-13 showing the differences in current decay between each of the wavelengths used.

The figure 5-14 shows that when discharging the thin film YBCO using five different wavelengths. The rates of decay are different, but each discharge still approaches a similar

asymptotic current. This result could indicate that a more energetic photon disrupts a greater number of Cooper pairs. Even though there is a trend in the decay rates, the error in the measurements (Figure 5-15) are too great to make a determination.

If the trend in decay rates were to continue, a 400 nm wavelength light would induce a much greater decay rate in the current than a 750 nm laser. A Barium Borate (BBO) crystal, a frequency doubler, was used to create 400 nm laser pulses from the 800 nm Ti:Sapphhire laser. The results did not follow the trend set by the previous experiment. The 400 nm beam decayed the current at a slower rate than the 900 nm beam.
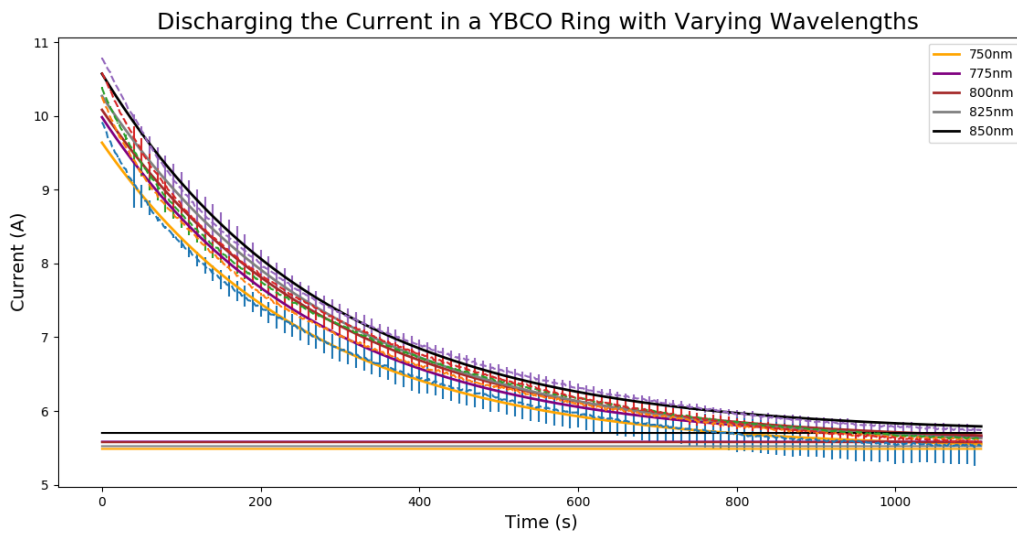

Figure 5-15. Plot of the current decay using various wavelengths along with standard deviation.
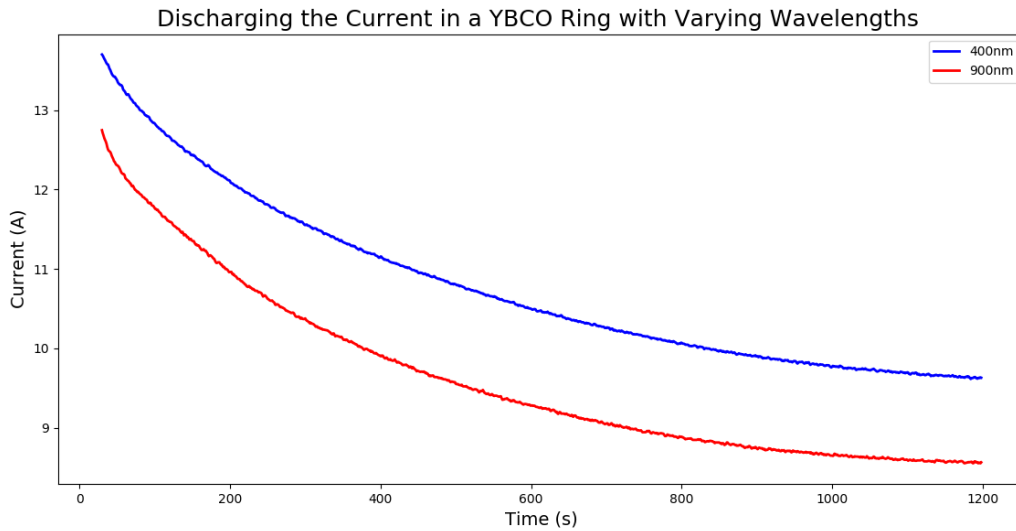
Figure 5-16. When comparing the 400 nm beam to the 900 nm beam they did not follow the same trend as the previous experiment. The 400 nm beam had a time constant of -0.0021s and the 900 nm beam had a time constant of -0.0026s.

The varying rates are most likely due to spot size differences because of the different wavelengths. Equation 5.5 shows how the laser spot size is dependent on wavelength and focal length of the focusing optic, where w_f is the spot size, λ is the wavelength, f is the focal length of the focusing optic, and w_o is the beam waist of the laser.

$$w_f = \frac{\lambda f}{\pi w_0} \tag{5.5}$$

5.5 THz Generation and Detection Experiment

From the previous experiments we determined that the ultrafast Ti:Sappire pulsed laser is capable of depleting the current in the YBCO thin film. Combined with the picosecond response time shown from the pump-probe spectroscopy experiment there is a good chance that a pulsed laser depleted persistent current in YBCO is producing THz radiation. Multiple average powers were used ranging from 109 mW to 1.5 W, but no THz was detected. There are three possible

reasons as to why no THz was detected. The directionality of the YBCO thin film antenna is unknown, the polarization is unknown, and the energy per laser pulse is not high enough.

If the YBCO thin film antenna is not emitting THz radiation in the direction of parabolic mirror used to capture the radiation then none will be detected. It was noticed in YBCO discharging experiments performed at the Air Force Research Laboratories that the YBCO thin film emitted GHz radiation in all directions.

If the parabolic mirror is capturing THz radiation emitted by the YBCO thin film the Electro-optic detection setup might not be able to detect the radiation. Electro-optic detection is polarization based and the polarization of the potential THz radiation is unknown. The ZnTe used as the electro-optic detector was rotated to examine several polarization angles. Additionally the probe beam polarization was rotated 90 degrees to cover all angles.

In addition to the directionality and polarization issues the electro-optic detection might not be sensitive enough to detect any incoming THz radiation. Electromagnetic radiation generation is proportional to the change in current vs the change in time, $THz_{radiation} \propto \frac{d\vec{J}}{dt}$. In previous YBCO emission experiments the thin film persistent current was completely depleted with a single 47 fs laser pulse from an amplified Ti:Saphhire laser (Bullard, T J, et al., 2019). In these experiments the fastest time recorded for complete current depletion was 5s with a 1.5 W average power. The stark contrast in depletion times is due to the energy in each pulse. The Ti:Sapphire laser used in these experiments had anywhere between 0.5 nJ per pulse to 10 nJ per pulse. In the microwave experiments the Ti:Sapphire laser was amplified and a single pulse had 4 mJ per pulse.

6. Summary and Future Work

While the persistent current in the YBCO annulus was depleted in our experiments we were not able to detect THz radiation. As previously stated the energy per pulse may have been too low to produce a detectable amount of THz. An amplified laser with a lower repetition rate, 80 MHz in these experiments, could have enough energy per pulse to generate detectable THz using our time domain setup. Even a different experimental setup using a THz horn antenna, such as Bulmer et al., could be used to verify that THz is being produced by depleting a persistent current. Their experiment required a pulsed laser with a pulse picker to single out an individual pulse and detect microwave radiation emitted from each laser pulse.

For the magnetic charging experiments we used a spherical neodymium magnet to induce a persistent current on the YBCO annulus which presented its own problems. The magnet was placed on a micrometer stage and gradually moved into position until the desired magnetic field was detected by a hall probe which was centered under the substrate. An electromagnet/solenoid might be an improvement over this method since the magnetic field could be easily controlled with a DC current generator.

An electromagnet would also be an improvement due to its shape. A spherical neodymium magnet was used which creates a magnetic field which is not perpendicular to the surface of the YBCO annulus used in these experiments. An electromagnet with a permanently placed in line with the annulus would have been optimal. This was our original intent when we attempted to use a cryostat. An electromagnet was placed directly behind the cryostat, however we were not able to induce a persistent current when the YBCO was in the cryostat.

As previously discussed it was believed the cryostat was not reducing the temperature of the YBCO annulus below its critical temperature due to potential temperature gradient formed

from the amount of interfaces heat would have to transfer through. If liquid helium were used the temperature gradient could have been overcome.

7. Works Cited:

Reports and Data. "Lightweight Materials Market to Reach USD 276.81 Billion by 2027: Reports and Data." *GlobeNewswire News Room*, Reports and Data, 9 June 2020, https://www.globenewswire.com/news-release/2020/06/09/2045796/0/en/Lightweight-Materials-Market-To-Reach-USD-276-81-Billion-By-2027-Reports-and-Data.html.

Tani, Masahiko, et al. "Generation and Detection of Terahertz Pulsed Radiation with Photoconductive Antennas and Its Application to Imaging." *Measurement Science and Technology*, vol. 13, no. 11, 2002, pp. 1739–1745., doi:10.1088/0957-0233/13/11/310.

D. H. Auston, "Subpicosecond electro-optic shock waves," Appl. Phys. Lett. 43, 713–715 (1983).

C. Fattinger and D. Grischkowsky, "Point source terahertz optics," Appl. Phys. Lett. 53, 1480–1482 (1988).

Harmon, E. S., et al. "Carrier Lifetime versus Anneal in Low Temperature Growth GaAs." *Applied Physics Letters*, vol. 63, no. 16, 1993, pp. 2248–2250., doi:10.1063/1.110542.

Burford, Nathan M., and Magda O. El-Shenawee. "Review of Terahertz Photoconductive Antenna Technology." *Optical Engineering*, vol. 56, no. 1, 2017, p. 010901., doi:10.1117/1.oe.56.1.010901.

Apostolopoulos, V, and M E Barnes. "THz Emitters Based on the Photo-Dember Effect." *Journal of Physics D: Applied Physics*, vol. 47, no. 37, 2014, p. 374002., doi:10.1088/0022-3727/47/37/374002

Matsushita T. (2007) Flux Pinning Mechanisms. In: Flux Pinning in Superconductors. Springer,

    Berlin, Heidelberg. https://doi.org/10.1007/978-3-540-44515-9_6

Wu, Q., et al. "Broadband Detection Capability of ZnTe Electro-Optic Field Detectors." *Applied Physics*

    Letters, vol. 68, no. 21, 1996, pp. 2924–2926., doi:10.1063/1.116356.

Karpowicz, N., et al. "Compact Continuous-Wave Subterahertz System for Inspection Applications."

    Applied Physics Letters 86.5 (2005): 054105.

Seco-Martorell, C., et al. Goya's Artwork Imaging with Terahertz Waves. Vol. 21., 2013.

Clément Paradis, Jakub Drs, Norbert Modsching, Olga Razskazovskaya, Frank Meyer, Christian Kränkel,

    Clara J. Saraceno, Valentin J. Wittwer, and Thomas Südmeyer, "Broadband terahertz pulse

    generation driven by an ultrafast thin-disk laser oscillator," Opt. Express **26**, 26377-26384 (2018)

Benzi, Paola, et al. "Oxygen Determination from Cell Dimensions in YBCO Superconductors."

    Journal of Crystal Growth, vol. 269, no. 2-4, 2004, pp. 625–629.,

    https://doi.org/10.1016/j.jcrysgro.2004.05.082.

Tonouchi, M., et al. "Terahertz Emission Properties from Flux-Trapped Ybco Thin Films."

      Physica C: Superconductivity, vol. 293, no. 1-4, 1997, pp. 82–86.,

      https://doi.org/10.1016/s0921-4534(97)01519-0.

Lewis, R A. "A Review of Terahertz Detectors." *Journal of Physics D: Applied Physics*, vol. 52,

    no. 43, 2019, p. 433001., https://doi.org/10.1088/1361-6463/ab31d5.

Tinkham, Michael. *Introduction to Superconductivity*. Dover Publications, 2015.

Delft, Dirk Van, and Peter Kes. "The Discovery of Superconductivity." *Physics Today*, vol. 63,

no. 9, 2010, pp. 38–43., doi:10.1063/1.3490499.

Meissner, W., and R. Ochsenfeld. "Ein Neuer Effekt Bei Eintritt Der Supraleitf Higkeit." *Die*

Naturwissenschaften, vol. 21, no. 44, 1933, pp. 787–788., doi:10.1007/bf01504252.

De Gennes, P. (1999). Superconductivity Of Metals And Alloys. Boca Raton: CRC Press,

https://doi.org/10.1201/9780429497032

White, Guy Kendall., and Philipp J. Meeson. *Experimental Techniques in Low-Temperature*

Physics. 4th ed., Clarendon Pr., 2006.

Bardeen, J., et al. "Theory of Superconductivity." *Physical Review*, vol. 108, no. 5, 1957, pp.

1175–1204., doi:10.1103/physrev.108.1175.

Landau Lev Davydovič, and Pitaevskij Lev Petrovič. *Statistical Physics: Part 2*. Pergamon

Press, 1981.

Kadin, Alan M. *Introduction to Superconducting Circuits*. Wiley, 1999.

"Fluctuations of the Order Parameter." *Statistical Physics: Part 1*, by Landau Lev Davidovič.

and Lifšic Evgenij Michajlovič., Pergamon Press, 1980, pp. 471–478.

Bardeen, John, and M. J. Stephen. "Theory of the Motion of Vortices in Superconductors."

Physical Review, vol. 140, no. 4A, 1965, https://doi.org/10.1103/physrev.140.a1197.

Wu, M. K., et al. "Superconductivity at 93 K in a New Mixed-Phase Y-Ba-Cu-O Compound System at Ambient Pressure." *Physical Review Letters*, vol. 58, no. 9, 1987, pp. 908–910., doi:10.1103/physrevlett.58.908.

Varshney, Dinesh. (2011). Alkaline Earth (Ca) and Transition Metal (Ni) Doping on The Transport Properties Of Y1-Xcaxba2(Cu1-Yniy)3O7-delta Superconductors. Journal of Modern Physics. 2. 922-927. 10.4236/jmp.2011.28109.

Prozorv, R, et al. "Measurements of the Absolute Value of the Penetration Depth in High-T c Superconductors Using a Tunnel Diode Resonator." *ArXiv:Cond-Mat/0007013v1 [Cond-Mat.supr-Con]*, 2 July 2000, doi:10.1063/1.1328362.

Johnston, Michael B., and Laura M. Herz. "Hybrid Perovskites for Photovoltaics: Charge-Carrier Recombination, Diffusion, and Radiative Efficiencies." *Accounts of Chemical Research*, vol. 49, no. 1, 2015, pp. 146–154., doi:10.1021/acs.accounts.5b00411.

Bullard, T J, et al. "Microwave Antenna Properties of an Optically Triggered Superconducting Ring." *Superconductor Science and Technology*, vol. 32, no. 12, 2019, p. 125012., https://doi.org/10.1088/1361-6668/ab48ce.

"Index of Refraction of Saturated Liuid Nitrogen." *Thermophysical Properties of Nitrogen from the Fusion Line to 3500 R (1944 K) for Pressures to 150,000 Psia (10342 x $10^5 N/m^2$)*, by Richard T. Jacobsen, National Bureau of Standards, 1973, pp. 20–20.

Fan, Y.x., et al. "Barium Borate Optical Parametric Oscillator." *IEEE Journal of Quantum Electronics*, vol. 25, no. 6, 1989, pp. 1196–1199., doi:10.1109/3.29247.

Malitson, I. H. "Interspecimen Comparison of the Refractive Index of Fused Silica*,†." *Journal of the Optical Society of America*, vol. 55, no. 10, 1965, p. 1205., https://doi.org/10.1364/josa.55.001205.

ZHAO, G. L., and D. BAGAYOKO. "A Proposed New Measurement of the Superconducting Gap in YBA2CU3O7." *International Journal of Modern Physics B*, vol. 21, no. 18n19, 2007, pp. 3290–3293., https://doi.org/10.1142/s0217979207044391.

Segre, Gino P. "Pump Probe Spectroscopy of Quasiparticle Dynamics in Cuprate Superconductors." 2001, doi:10.2172/787131.

M. N. Polyanskiy, "Refractive index database," *https://refractiveindex.info*. Accessed on 2019-09-03.

*Mannella, N.; et al. (2005). "Nodal quasiparticle in pseudogapped colossal magnetoresistive manganites". Nature. **438** (7067): 474–478. arXiv:cond-mat/0510423. Bibcode:2005Natur.438..474M. doi:10.1038/nature04273. PMID 16306987.*